Research Article | Vol. 28, No. 23 / 9 November 2020 / Optics Express 34147
Optics EXPRESS

# Drivers of spectral optical scattering by particles in the upper 500 m of the Atlantic Ocean

EMANUELE ORGANELLI,[1,2,*] GIORGIO DALL'OLMO,[1,3] ROBERT J. W. BREWIN,[1,4] FRANCESCO NENCIOLI,[1] AND GLEN A. TARRAN[1]

[1]Plymouth Marine Laboratory, Prospect Place, The Hoe, PL1 3DH Plymouth, UK
[2]National Research Council (CNR), Institute of Marine Sciences (ISMAR), Via Fosso del Cavaliere 100, 00133 Rome, Italy
[3]National Centre for Earth Observation, Plymouth Marine Laboratory, Prospect Place, The Hoe, PL1 3DH Plymouth, UK
[4]University of Exeter, College of Life and Environmental Sciences, Penryn Campus, Cornwall TR10 9FE, UK
*emanuele.organelli@cnr.it

**Abstract:** Optical models have been proposed to relate spectral variations in the beam attenuation ($c_p$) and optical backscattering ($b_{bp}$) coefficients to marine particle size distributions (PSDs). However, due to limited PSD data, particularly in the open ocean, optically derived PSDs suffer from large uncertainties and we have a poor empirical understanding of the drivers of spectral $c_p$ and $b_{bp}$ coefficients. Here we evaluated PSD optical proxies and investigated their drivers by analyzing an unprecedented dataset of co-located PSDs, phytoplankton abundances and optical measurements collected across the upper 500 m of the Atlantic Ocean. The spectral slope of $c_p$ was correlated ($r>0.59$) with the slope of the PSD only for particles with diameters >1 µm and also with eukaryotic phytoplankton concentrations. No significant relationships between PSDs and the spectral slope of $b_{bp}$ were observed. In the upper 200 m, the $b_{bp}$ spectral slope was correlated to the light absorption by particles ($a_p$; $r<-0.54$) and to the ratio of cyanobacteria to eukaryotic phytoplankton. This latter correlation was likely the consequence of the strong relationship we observed between $a_p$ and the concentration of eukaryotic phytoplankton ($r=0.83$).



## 1. Introduction

Microscopic organic particles play a key role in the ocean biological carbon pump, transferring carbon from the surface to the deep ocean [1], which helps modulate the Earth's climate [2,3]. These particles encompass a variety of living organisms (i.e., viruses, bacteria, phytoplankton and zooplankton) and detrital matter (e.g., debris and faecal pellets) that vary in concentration, size and composition, both spatially and temporally. Understanding the variability in particle concentration, size distribution and composition is of paramount importance to accurately estimate the magnitude of global carbon fluxes [4,5].

The Particle Size Distribution (PSD) is defined as the concentration of marine particles within a given size class and is often approximated as a power law function of the diameter (D; units of µm):

$$N(D) = N_0 \left(\frac{D}{D_0}\right)^{-\xi}, \quad (1)$$

#408439 https://doi.org/10.1364/OE.408439
Journal © 2020 Received 27 Aug 2020; revised 14 Oct 2020; accepted 15 Oct 2020; published 27 Oct 2020

Optics EXPRESS

where N(D) is the number of particles per volume within a given diameter bin (units of $m^{-3}$ $\mu m^{-1}$), $N_0$ is the concentration of particles at the reference diameter ($D_0$), and $\xi$ is the dimensionless slope of the distribution.

One common method to measure the PSD is through an electrical impedance particle sizer such as the Coulter Counter [6]. This instrument counts and sizes particles based on changes in the electrical field generated through an aperture across which the particle suspension is forced, without distinguishing between living or detrital particles. Flow cytometry can be used as a complementary technique to help resolve the composition of the particles. It can be used to distinguish phytoplankton groups from detritus over a broad size range by exploiting the natural fluorescence properties of individual phytoplankton cells [7]. Both these techniques have an invaluable analytic power, but are discrete measurements, involving specialized equipment and trained operators. Consequently, they are not well-suited to capture high spatial and temporal variations in particle size and composition.

To increase the temporal and spatial resolutions with which we observe marine particles, optical scattering has been proposed as a monitoring tool [8–13]. Measurements of the particulate beam attenuation ($c_p$) and optical backscattering ($b_{bp}$) coefficients offer the crucial advantage to be acquired continuously on ships [14,15] and moorings [16], using autonomous profiling platforms [17,18], as well as from space through ocean color remote sensing [10,19]. Measuring $c_p$ and $b_{bp}$ coefficients provides an opportunity to observe, in a systematic way, the dynamics of marine particles from the surface to the ocean interior.

Spectral variations in $c_p$ and $b_{bp}$ (units of $m^{-1}$) have been approximated as a power law function of the wavelength ($\lambda$; units of nm):

$$c_p(\lambda) = c_p(\lambda_0)\left(\frac{\lambda}{\lambda_0}\right)^{-\gamma}, \tag{2}$$

and

$$b_{bp}(\lambda) = b_{bp}(\lambda_0)\left(\frac{\lambda}{\lambda_0}\right)^{-\eta}, \tag{3}$$

where $c_p(\lambda_0)$ and $b_{bp}(\lambda_0)$ are the coefficients at the reference wavelength ($\lambda_0$), and $\gamma$ and $\eta$ are the dimensionless slopes of the $c_p$ and $b_{bp}$ coefficients, respectively.

Assuming that the size distribution of a population of marine particles can be approximated by Eq. (1), studies have suggested that as the slope $\xi$ decreases, so do $\gamma$ and $\eta$ [8–11,13]. Hence, $\gamma$ and $\eta$ have been proposed as proxies to estimate $\xi$, and bio-optical models relating $\xi$ to $\gamma$ or $\eta$ have been developed [9,11]. However, these models suffer from large uncertainties in open-ocean surface waters [15]. These uncertainties are unknown for the mesopelagic zone of the ocean (i.e., 200-1000 m) where no PSD data are available to the best of our knowledge. These gaps arise from limited oceanographic sampling of PSDs, meaning we cannot validate model outputs [11] and have a poor understanding of other factors that may influence the relationships between optical proxies ($\gamma$ or $\eta$) and PSD. Coincident measurements of spectral optical properties, flow cytometry and particle size distributions, as a function of depth and trophic regimes, are needed to fill these gaps.

Here, we analyze an unprecedented dataset of co-located particle size distributions (from a Coulter Counter), phytoplankton abundances and composition (from flow cytometry), and spectral $c_p$ and $b_{bp}$ coefficients collected in the upper 500 m of the Atlantic Ocean during two Atlantic Meridional Transect (AMT) expeditions. We focus on the size and composition of the encountered particle populations, and on descriptors of the size distribution (i.e., $\xi$). We then relate $\xi$ to $\gamma$ and $\eta$, evaluate previously established bio-optical models, and investigate the influence of particle composition and light absorption on $\gamma$ and $\eta$.

Optics EXPRESS

## 2. Material and methods

### 2.1. Study area and sampling platforms

Measurements of optical properties and particle abundances and characteristics were acquired during two AMT expeditions carried out in October-November 2012 (AMT22) and September-November 2016 (AMT26) (Fig. 1). Both transects started in the United Kingdom and ended in Chile (AMT22) and the Falkland Islands (AMT26), and encompassed various trophic regimes with chlorophyll concentration ([Chl]) spanning a range from 1 mg $m^{-3}$ to values ≤0.03 mg $m^{-3}$ in the oligotrophic subtropical gyres (Fig. 1).

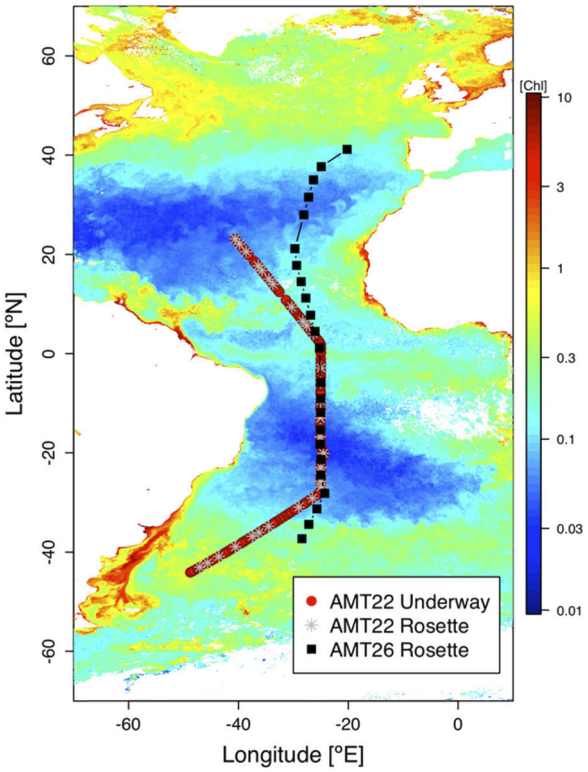


**Fig. 1.** Stations sampled during AMT22 using the ship's flow-through underway system (circle), and AMT22 (star) and AMT26 (square) using the rosette sampler. Stations are superimposed onto the October 2016 Ocean Colour ESA Climate Change Initiative (v3.1) monthly Chlorophyll concentration ([Chl], units of mg $m^{-3}$) composite.

During AMT22, 134 samples of co-located PSD, spectral $c_p$ and particulate light absorption ($a_p$) coefficients were obtained from the 5 m underway clean seawater supply of the ship acquired in flow-through mode (Fig. 1). Spectral $b_{bp}$ coefficients and flow cytometry samples were collected at 5 m depth during the upcast of a rosette sampler equipped with 24 × 20-L Niskin bottles. A Sea-bird Scientific SBE 9 Conductivity-Temperature-Depth (CTD) sensor provided vertical profiles of temperature and salinity. A total of 31 $b_{bp}$ and flow cytometry measurements acquired within a 1 h window from the underway system sampling were retained (Fig. 1).

On AMT26, PSD and flow cytometry samples were acquired at 23 stations using a similar rosette sampler as used on AMT22 (Fig. 1). Samples were acquired during the upcast at five depths (5, 150/200, 300/375, 400/450, and 500 m) in addition to the depth of the deep chlorophyll maximum (DCM) as identified by an AquaTracka III fluorometer (Chelsea Technologies Group Ltd). Flow

Optics EXPRESS

cytometry measurements were limited to the upper 200 m. In the upper 200 m, water samples were also acquired at individual depths to measure the spectral light absorption coefficients by colored dissolved organic matter ($a_{CDOM}$). A Sea-bird Scientific SBE 9 Conductivity-Temperature-Depth (CTD) sensor provided vertical profiles of temperature and salinity. The rosette sampler was also equipped to collect 0-500 m profiles of spectral optical backscattering coefficients. Only profiles acquired during the upcast were retained because they were the closest to water sampling. At the same time of the water sampling, 0-250 m profiles of the spectral beam attenuation and light absorption coefficients by particles were independently collected through an optics rig.

### 2.2. Particle size distribution and descriptors

The protocols used for measuring the particle size distribution (units of particles $m^{-3}$ $\mu m^{-1}$) are detailed in Organelli et al. [20]. Briefly, during both cruises, seawater samples were measured on board immediately after sampling, by means of a Multisizer III Coulter Counter (Beckman Coulter). The Coulter Counter was fitted with a 70 µm aperture during AMT22, and with 20 µm and 100 µm apertures on AMT26. Hence, the measured size ranges of equivalent spherical diameters (ESDs) were 1.4–42 µm, 0.588–12 µm and 2–60 µm for 70, 20 and 100 µm apertures, respectively. ESDs were distributed in 200 and 256 logarithmically spaced size bins on AMT22 and AMT26, respectively. All apertures were calibrated using bead suspensions before and during the cruises [20]. On both cruises, blank references of filtered seawater were recorded daily for each aperture [20].

Samples were repeated on both cruises. On AMT22, 2 mL samples were replicated from 2 to 26 times. During AMT26, 50 µL and 1 mL replicates were acquired for 20 and 100 µm apertures, respectively. Samples were replicated from 3 to 15 times in order to achieve an error <15% around 3 µm and 6 µm for 20 µm and 100 µm apertures, respectively [20]. All replicates for each aperture were finally summed to obtain PSDs. For AMT26 samples, the PSDs obtained from the 20 and 100 µm apertures were then combined into a single measurement by merging the two PSDs at around 2.14 µm where they presented similar bin widths and upper/lower bin limits. The resulting PSD consisted of 360 logarithmically spaced bins distributed between 0.588 and 60 µm. For all AMT22 and AMT26 PSDs (n=268), the uncertainty of measurements within each size bin was calculated by propagation of the error [21] due to the number of particles, the blank reference and the Multisizer III volumetric pump accuracy [20].

For each measured PSD, the dimensionless slope of the distribution $\xi$ was obtained from fitting Eq. (1) in logarithmic space. In particular, $\xi$ was estimated through Monte Carlo simulations (n=1000) by randomly sampling, within each size bin, normally distributed PSD values within twice the measured standard deviation (i.e., 95% confidence level). For each measured PSD, the resulting $\xi$ was the median value of all simulated regression slopes. PSD slopes were computed over the full measured size range (i.e., 1.4-42 µm for AMT22 and 0.588-60 µm for AMT26), and named $\xi_{1.4-42}$ and $\xi_{0.59-60}$ for AMT22 and AMT26, respectively. Specific to AMT26, $\xi$ was also calculated for particles with diameters between 0.588 and 1.14 µm ($\xi_{0.59-1.14}$), and for those ranging between 1.14 and 60 µm ($\xi_{1.14-60}$). The threshold at 1.14 µm was chosen to include prokaryotic phytoplankton (i.e., the genera *Synechococcus* and *Prochlorococcus*) within the fraction of smallest particles [22]. This threshold was also consistent with changes in measured PSD slopes as observed around 1 µm (see Results). The concentrations of particles (units of $m^{-3}$) for various size ranges were derived by integrating the measured PSDs within the given size ranges. Finally, the area concentration of equivalent spherical particles (units of $\mu m^2$ $m^{-3}$ $\mu m^{-1}$) was computed by multiplying the particle concentration within each size bin for the particle cross-sectional area at the central diameter of the given bin and divided for the bin width.

Optics EXPRESS

### 2.3. Phytoplankton abundance and composition

On both AMT22 and AMT26, a Becton Dickinson FACSort flow cytometer equipped with an air-cooled laser emitting blue light at 488 nm measured the abundance and structure of phytoplankton communities [23]. Seawater samples were directly collected from Niskin bottles in 250 mL polycarbonate bottles and immediately analyzed for counting the two cyanobacteria *Prochlorococcus* sp. and *Synechococcus* sp., and pico- and nano-eukaryotic phytoplankton cells on the basis of their auto-fluorescence and light scattering properties [23,24]. Coccolithophores and cryptophytes were enumerated separately from nano-eukaryotes [23]. Heterotrophic bacteria were also counted on a sub-sample of water collected from the rosette sampler that was immediately fixed with glutaraldehyde (paraformaldehyde on AMT22) solution (Sigma-Aldrich, 50%, Grade 1. 0.5% final concentration) at 4°C for 30 min. Samples were then stained for 1 h at room temperature in the dark with the DNA stain SYBR Green I (Thermo-Fisher) to distinguish bacteria from the other suspended particles, and finally analyzed with the flow cytometer [24]. In this study, we refer to cyanobacteria as the sum of abundances of *Prochlorococcus* sp. and *Synechococcus* sp., to prokaryotes as the sum of abundances of cyanobacteria and heterotrophic bacteria, and to eukaryotes as the sum of abundances of all pico- and nano-eukaryotic phytoplankton including coccolithophores and cryptophytes.

### 2.4. Optical properties and proxies of particle size

Spectral measurements of the bulk beam attenuation coefficient were acquired by an ac-s spectrophotometer (WETLabs, Seabird-Scientific) on AMT22, and using an ac-9 spectrophotometer (WETLabs, Seabird-Scientific) on AMT26. The measurements acquired by the ac-s and ac-9 are comparable due to the same optical configuration of the instruments, beam acceptance angle [25], and path length (25 cm). The ac-s data were interpolated to 151 wavelengths between 450 and 750 nm every 2 nm. The ac-9 collected data at 9 bands (i.e., 412, 440, 488, 510, 532, 554, 650, 676, 715 nm). On both cruises, measurements were also acquired after filtration through a 0.2-μm filter to evaluate the contribution of the colored dissolved organic matter, and calibration drifts. The 0.2 μm filtered signal was then subtracted from the bulk signal to obtain the spectral beam attenuation coefficients of particles ($c_p$) according to established protocols [26].

The ac-s and ac-9 measurements of light absorption before and after 0.2 μm filtration were also used to compute the spectral particulate light absorption coefficients ($a_p$). On the $a_p$ data, a scattering correction was applied [27]. The spectral particulate scattering coefficients ($b_p$) were then derived by subtracting $a_p$ from $c_p$. Spectral light absorption coefficients by colored dissolved organic matter ($a_{CDOM}$) were measured on board immediately after water sampling using a liquid waveguide capillary cell system (LWCC; 3000 series, World Precision Instruments) following protocols detailed in Dall'Olmo et al. [28]. Measurements were collected using a path length of 1 m within the spectral range 350-750 nm. The total light absorption coefficient ($a_{tot}$) was obtained as the sum of $a_p$, $a_{CDOM}$ and the light absorption by pure seawater ($a_w$) as given by Pope and Fry [29].

Optical backscattering coefficients were acquired during the upcast of the rosette used for water sampling by a HydroScat-6P (HOBILabs) sensor. This sensor acquired, every 0.3 m, the angular scattering coefficients $\beta$ at a central angle of 140° and five wavelengths (i.e., 442, 488, 550, 620, and 671 nm). At each wavelength, $\beta$ was converted into the particulate angular scattering coefficient $\beta_p$ by removing the contribution of pure seawater which in turn depends on temperature and salinity [30]. Then, $\beta_p$ was converted into $b_{bp}$ following established protocols and applying a $\chi$ factor equal to 1.14 [31,32]. The $b_{bp}$ vertical profiles were smoothed with a moving-median filter (5 point window) and finally binned at 1 m resolution. HydroScat- 6P measurements were analyzed using manufacturer calibration. Moreover, an inter-comparison between HydroScat-6P measurements and those simultaneously acquired by a WETLabs ECO-BB3 (Seabird-Scientific) sensor showed high consistency, verifying the quality of these measurements [20].

Optics EXPRESS

Optical backscattering measurements acquired by the HydroScat-6P sensor may require a correction for attenuation of light called σ-correction [31]. Following HOBILabs [31], the correction factor $K_{bb}$ was computed from independent $a_p$, $a_{CDOM}$ and $b_p$ measurements acquired as described above. Because we used discrete $a_{CDOM}$ values, this correction was developed only using 43 samples distributed between 0 and 200 m along all the AMT26 transect. At each wavelength, estimated $K_{bb}$ values were lower for the mesopelagic than upper water column samples, and the mean values are reported in Supplement 1, Table S1. To test the potential impact of the σ-correction on the whole database, the average $K_{bb}$ values were applied to all measured uncorrected $b_p$ coefficients (i.e., n=134). The σ-correction increased $b_{bp}$ values. The increase was the highest for $b_{bp}$ values at 442 nm (4.2 ± 1.2%) while it decreased to 0.67 ± 0.16% at 671 nm (Supplement 1, Table S1). In agreement with previous studies in clear waters [32,33], the impact of the σ-correction on the derived optical backscattering coefficients was therefore negligible. As a consequence, analyses were pursued only on $b_{bp}$ values to which no σ-correction was applied. Such a choice also avoided making assumptions on σ-correction for samples without coincident $a_{CDOM}$ measurements, and thus allowed us to exploit the entire database of co-located PSDs and $b_{bp}$ measurements, including also those acquired on AMT22.

For each measured $c_p$ coefficient, the dimensionless slope of the spectrum γ was obtained by fitting Eq. (2) in logarithmic space. To compare with data from the literature, γ was computed for the entire spectral ranges measured [9,13]. For each measured $b_{bp}$ coefficient, we computed the slope of the spectrum η over two different spectral ranges: i) $\eta_{488-550}$ was computed as the ratio in log-space between the bands 488 and 550 nm following Antoine et al. [16], in order to use the same spectral range of, and compare the results with, a previously established bio-optical model specifically developed for space-based applications [11]; and ii) $\eta_{442-671}$ was computed by fitting Eq. (3) in log-space over the entire measured spectral range (i.e., 442-671 nm). Then, AMT26 values of γ, $\eta_{488-550}$ and $\eta_{442-671}$, and AMT22 values of $\eta_{488-550}$ and $\eta_{442-671}$ were calculated from 1 m resolution vertical profiles as the median of the slopes estimated in a window of 5 m centered at the depth of PSD samples. Only for AMT22, the median value of γ was acquired in a window of 5 minutes corresponding to the time of the PSD water sampling.

### 2.5. Statistics

All comparisons were evaluated using the Pearson's correlation coefficient (r) of a linear fit, whose significance was tested on a two-tailed Student's *t*-test. Statistics were calculated on log-transformed quantities of particle concentrations and ratios, and light absorption coefficients [34]. The root mean square error of prediction (RMSE) and the median percent difference (MPD) were calculated as follows:

$$RMSE = \sqrt{\frac{\sum_{i=1}^{n} \left(x_{i,estimated} - x_{i,measured}\right)^2}{n}}, \tag{4}$$

and

$$MPD = median\left(100^* \left|\frac{x_{i,estimated}}{x_{i,measured}} - 1\right|\right), \tag{5}$$

respectively, where $x_i$ are estimated and measured variables, and $n$ is the number of observations.

## 3. Results

### 3.1. Shape of the PSDs

The number concentration of particles decreased with increasing diameter (Fig. 2; Supplement 1, Figs. S1 and S2). At the surface and at the DCM, PSDs showed peaks in the submicron range around 0.7-0.8 µm, between 1 and 2 µm and less frequently above 5 µm (Fig. 2; Supplement 1,

Optics EXPRESS

Fig. S2). In addition, in the submicron range, peaks centered around 0.6 µm were also observed in some PSDs at the surface and at the DCM, even though these peaks could not be fully resolved because of the detection limits of the Coulter Counter (Fig. 2). In the mesopelagic zone, PSDs were generally featureless (Fig. 2; Supplement 1, Fig. S1). All PSDs at the surface and DCM showed low uncertainties within each size bin up to 5 µm for AMT26 and up to 7 µm for AMT22, while uncertainty increased for PSDs collected in the mesopelagic zone (Supplement 1, Fig. S3). Additional examples of PSDs with associated uncertainty from both AMT22 and AMT26 cruises can be found in Organelli et al. [20].

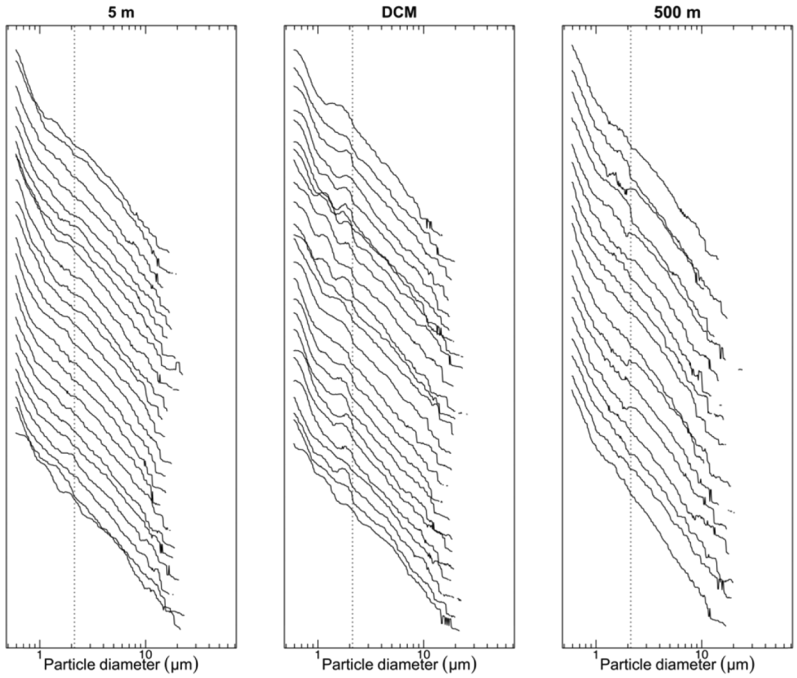


**Fig. 2.** Particle Size Distributions (PSDs) collected during the AMT26 cruise at the following depths: 5 m, deep chlorophyll maximum (DCM) and 500 m. In each panel, PSDs are shown in log-log scale. To improve visualization, PSDs have been spaced and smoothed with a moving-median filter (fifteen point window). Dashed vertical lines indicated the lower and upper limits of the size bin at which the PSDs acquired with the Coulter Counter's tube apertures of 20 µm and 100 µm diameters were merged.

The mean area concentration of equivalent spherical particles generally decreased with increasing diameter (Fig. 3). For samples at the DCM, besides the not-fully resolved peak around 0.6 µm, two additional clear peaks, likely due to pico-eukaryotes, were observed between 1 and 2 µm. For surface AMT22 samples, the area concentration was higher than for samples collected on AMT26 though with a larger variability (Fig. 3).

The power-law fit on the whole measured size range was insensitive to the observed peaks of particles and to the size distribution of submicron particles (Fig. 4). For AMT26 samples, the mean (± standard deviation) slope computed over the entire size range, $\xi_{0.59-60}$, was $3.4 \pm 0.3$ (n=134) while the slope of the distribution of measured submicron particles, $\xi_{0.59-1.14}$, was $6.0 \pm 1.0$ (Figs. 4 and 5). This $\xi_{0.59-1.14}$ slope was also driven by the poorly-resolved peak at 0.6 µm, likely due to *Prochlorococcus*. No significant correlation was observed among $\xi_{0.59-60}$ and $\xi_{0.59-1.14}$ (Supplement 1, Fig. S4(a)), while $\xi_{0.59-60}$ was significantly correlated with the slope of particles above 1.14 µm ($\xi_{1.14-60}$; Supplement 1, Fig. S4(b)). The average value of

Optics EXPRESS

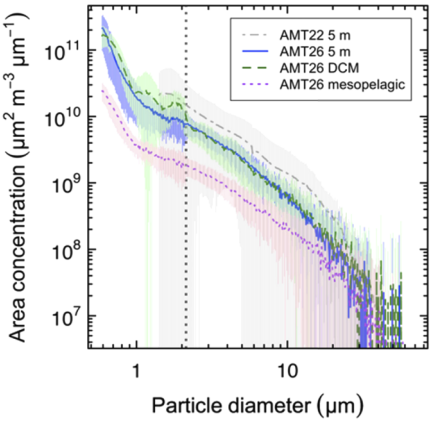


**Fig. 3.** Mean area concentrations for samples collected during the AMT22 cruise at 5 m depth (n=134), and on the AMT26 cruise at 5 m (n=23), at the depth of the deep chlorophyll maximum (DCM; n=25) and in the mesopelagic region (n=86). Error bars represent one standard deviation. The dashed vertical line indicates the size bin at which the PSDs acquired with apertures of 20 μm and 100 μm diameter were merged. AMT22 PSDs were collected between 1.4–42 μm.

$\xi_{1.14-60}$ was close (3.22 ± 0.23, n=134) to that describing the whole size range (Fig. 5(a)). The average slope for PSDs collected during AMT22 between 1.4 and 42 μm, $\xi_{1.4-42}$, was 3.38 ± 0.44 (n=134), and thus close to AMT26 $\xi_{0.59-60}$ and $\xi_{1.14-60}$ values (Fig. 5(a)).

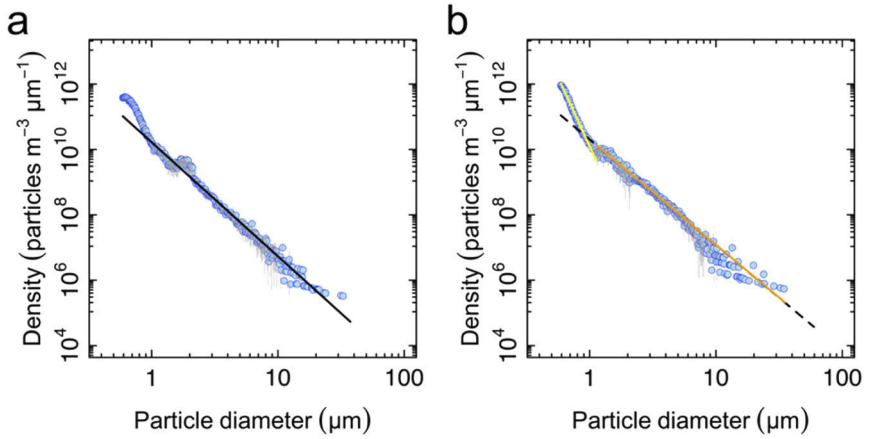


**Fig. 4.** Examples of how particle size distributions cannot be described by a single slope. (a) The power law fit (solid line) is calculated over the whole measured size range (0.59-60 μm); (b) The power law fit (dashed line) is calculated over the whole measured size range (0.59-60 μm), and for particle diameters between 0.59 and 1.14 μm (yellow solid line) and between 1.14 and 60 μm (orange solid line). Error bars represent the combined uncertainty (95% confidence intervals) as propagated from the summation of multiple particle size distribution measurements (see methods).

The slope ξ varied from the surface to the mesopelagic zone (Fig. 5(b)). Large mean slopes computed over the entire size range were observed at the surface and at the DCM (3.5 ± 0.2, n=48), with the steepest mean slopes at the DCM (3.6 ± 0.2, n=25). Lower slopes characterized the particle populations in the mesopelagic zone (3.3 ± 0.3, n=86). The slopes ξ observed along

Optics EXPRESS

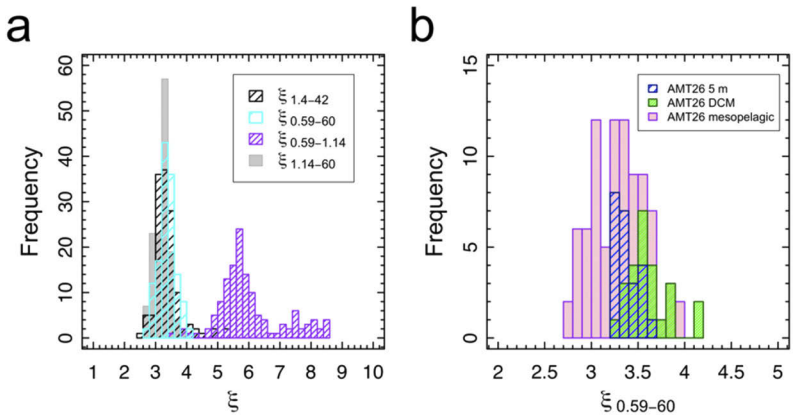


**Fig. 5.** (a) Frequency distributions of the slopes ξ estimated for all AMT22 and AMT26 samples (n=268). The slopes ξ were calculated over different ranges of particle sizes: 1.4-42 µm for AMT22 samples ($\xi_{1.4-42}$); and 0.59-60 µm ($\xi_{0.59-60}$), 0.59-1.14 µm ($\xi_{0.59-1.14}$) and 1.14-60 µm ($\xi_{1.14-60}$) for AMT26 samples; (b) Frequency distributions of the slopes $\xi_{0.59-60}$ for AMT26 samples grouped according to sampling depth.

the AMT transect were in agreement with expected oceanic values [13,35,36]. The slopes $\xi_{0.59-1.14}$ computed for the submicron range also decreased from 6.9 ± 1.0 (n=23) at the surface and 6.8 ± 1.6 (n=25) at the DCM, to 5.6 ± 0.4 (n=86) in the mesopelagic layer.

### 3.2. Phytoplankton and detritus contributions

The comparison between particle concentrations derived from PSD and flow cytometry measurements showed varying contributions of phytoplankton to the bulk particle population (Figs. 6 and 7). The concentrations of eukaryotic phytoplankton and of particles >1.14 µm were significantly correlated at the surface and at the DCM ($\log_{10}$(Eukaryotes) = 1.59(±0.09)*$\log_{10}$(Particles$_{1.14-60\ \mu m}$)-6.26(±0.87), r=0.90, p-value<0.01, n=79; Fig. 6(a)). At the DCM, eukaryotic phytoplankton represented at least half the pool of particles (Fig. 6(b)) with average relative contributions of 56 ± 16%. In contrast, non-phytoplanktonic particles >1.14 µm dominated at the other depths (Fig. 6(b)). The relative contributions of these detrital particles were 67 ± 19% and 95 ± 7% at the surface and in the mesopelagic zone, respectively. These values for detrital particles are consistent with previous estimations made for the southeast Pacific Ocean [37].

The concentrations of submicron particles were correlated with those of particles >1.14 µm (r=0.94, p-value<0.01, n=134; Fig. 7(a)), when the large range of concentrations from the ocean surface to the mesopelagic zone was considered. A significant correlation was also observed between the concentrations of submicron particles and cyanobacteria when including all samples (r=0.87, p-value<0.01, n=67), but due to the lower size limit of the Coulter Counter, PSDs underestimated these photosynthetic organisms (Fig. 7(b)). A better agreement on the 1:1 line with the Coulter Counter and cyanobacteria was found at the DCM where these organisms are larger and fluoresce more than at the surface [38]. Assuming low cyanobacteria abundances deeper than 200 m, the relative contributions of detritus with diameters <1.14 µm was calculated only for the mesopelagic region and was on average 93 ± 15% (Fig. 7(b)).

### 3.3. Spectral scattering and optical proxies of particle size

Measured spectral $c_p$ and $b_{bp}$ coefficients were consistent with previous measurements acquired in open-ocean waters [14,26,32,39]. The lowest $c_p$ and $b_{bp}$ values occurred for samples in the mesopelagic ocean (Fig. 8). No clear differences were observed for the values of $c_p$ and

Optics EXPRESS

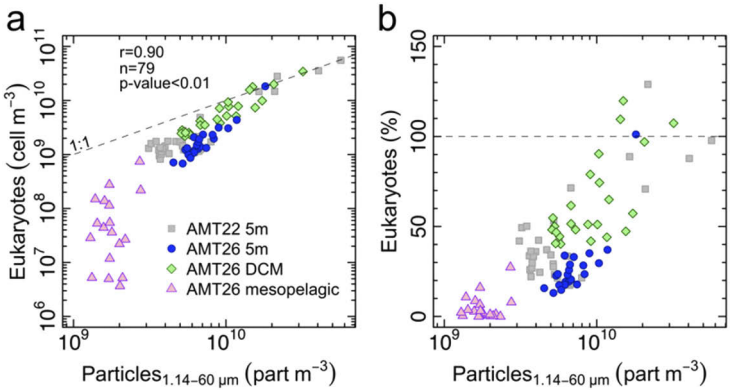


**Fig. 6.** (a) Comparison between cellular abundances of eukaryotic phytoplankton (from flow cytometry) and concentrations of particles with diameters >1.14 µm (from the Coulter Counter). The dashed line indicates the 1:1 ratio. Statistics for the linear fit on the log-transformed particle concentrations of samples at the surface and at the DCM level are reported. (b) Relative contributions of eukaryotic phytoplankton within populations of particles with diameters >1.14 µm *vs.* the concentrations of those particles. The dashed line indicates 100% of contribution by eukaryotic phytoplankton to the bulk particle population. In both panels, particle concentrations of AMT22 samples refer to the size range between 1.4 and 42 µm.

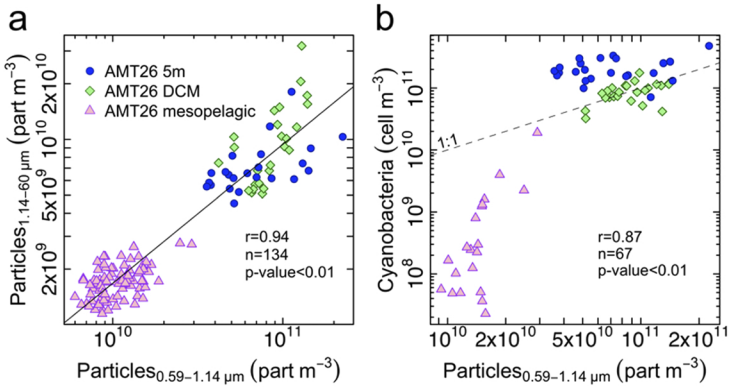


**Fig. 7.** (a) Comparison between concentrations of particles with diameters between 1.14 and 60 µm *vs.* those between 0.59 and 1.14 µm (from the Coulter Counter). The solid line is the linear fit on log-transformed quantities and statistics are shown. (b) Comparison between cellular abundances of cyanobacteria (from flow cytometry) and concentrations of particles with diameters <1.14 µm (from the Coulter Counter). The dashed line indicates the 1:1 ratio. Statistics for the linear fit on log-transformed particle concentrations are shown. In both panels, only samples collected during AMT26 are included.

$b_{bp}$ between the surface and the level of the DCM (Figs. 8(a) and (b)). The exception to this was for AMT22, where the samples collected at the end of the transect under high-chlorophyll concentrations (Fig. 1) showed the highest $c_p$ and $b_{bp}$ values of the whole dataset (Fig. 8).

The $c_p$ spectra measured on both AMT22 and AMT26 were relatively flat with values of $\gamma$ varying from 0.5 to 1.7 (on average 0.95 ± 0.20) regardless of depth (Fig. 8). This is in accordance with previous observations in the same area [26] and in other regions of the Atlantic Ocean [15]. Some features in the $b_{bp}$ spectra were sometimes observed, such as depressions at 488, 550 and

Optics EXPRESS

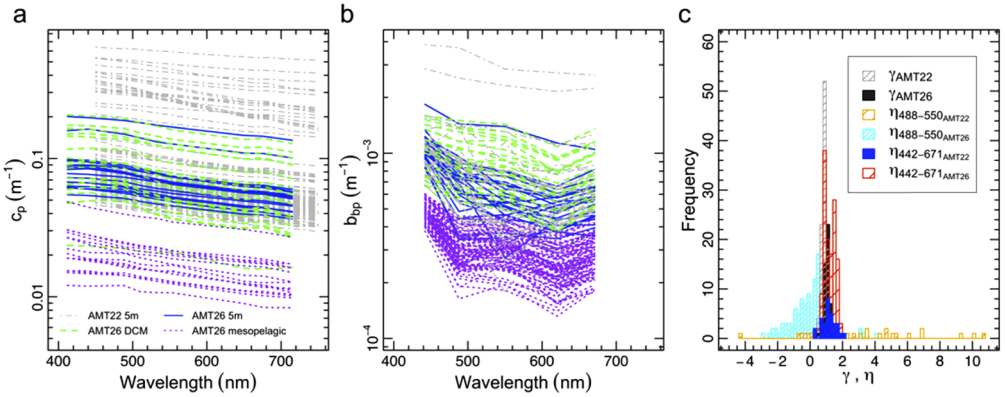


**Fig. 8.** Measured particulate spectral (a) beam attenuation ($c_p$) and (b) optical backscattering ($b_{bp}$) coefficients along the AMT22 and AMT26 transects, in the upper 500 m. (c) Frequency distributions of the slopes γ, $\eta_{488-550}$ and $\eta_{442-671}$ estimated for measured $c_p$ and $b_{bp}$ during AMT22 and AMT26 field expeditions.

620 nm (Fig. 8(b)). Similar features in $b_{bp}$ measurements acquired by a HydroScat- 6P meter have been observed in other regions of the global ocean [19,33]. As a consequence of such variability, the values of η varied strongly with the spectral range used for the computation (Fig. 8(c)). The values of $\eta_{488-550}$ ranged globally from -4.35 to 10.7, though we acknowledge that η values lower than -1.5 and higher than 5 have not been reported in the literature [11,13,16,26,33] and will therefore be excluded from the following analyses. The values of $\eta_{442-671}$ ranged from 0.24 to 2.09 (on average $1.20 \pm 0.35$). The range of $\eta_{442-671}$ values was in agreement with previous measurements along the same transect [26], as well as those acquired in other regions of the ocean [13,16,33]. The slope $\eta_{442-671}$ also increased with $b_{bp}(550)$, which is an indicator of seawater turbidity [33], though with different trends between surface samples and those collected at the other depths (Supplement 1, Fig. S5).

The relationship between the PSD slopes (ξ) computed over the entire size range and γ derived from spectral $c_p$ measurements was statistically significant, but with relatively large scatter (r=0.68, p-value<0.01, n=156; Fig. 9(a)). The measured ξ values were generally lower than those predicted using a bio-optical model based on $c_p$ [9], and yielded RMSE and MPD values equal to 0.62 and 18%, respectively. Consistency with this $c_p$-based model was observed only for samples collected at 5 m in chlorophyll-rich waters encountered at the end of the AMT22 transect (Fig. 9(a)). We must note that these samples collected during the AMT22 significantly influenced the observed relationship between ξ and γ as they encompassed a wider trophic range than waters encountered on AMT26. On AMT26, no optical scattering measurements co-located with PSDs were made south of 40°S where waters are rich in chlorophyll (Fig. 1).

No significant relationship was observed between the PSD slopes (ξ) and those derived from $b_{bp}$ at 488 and 550 nm, $\eta_{488-550}$ (Fig. 9(b)). Our observations for the upper 500 m of the Atlantic Ocean were close to the ξ predicted from a previously published model [11], but most of the samples collected at 5 m depth strongly departed from that model (Fig. 9(b)). Neither did we observe a significant relationship between ξ and $\eta_{442-671}$ when data from all depths were combined (r=-0.19, p-value=0.011, n=163; Fig. 9(c)). In this case, the previously established model [11] overestimated the measured ξ (RMSE=1.03, MPD=27%; Fig. 9(c)). Both γ, $\eta_{488-550}$ and $\eta_{442-671}$ were poorly or not correlated with the PSD slopes computed only for particles <1.14 µm (Supplement 1, Fig. S6). Finally, γ and $\eta_{442-671}$, were poorly correlated globally (Fig. 9(d)) and no correlation was found between γ and $\eta_{488-550}$ (r=-0.18, p-value=0.12, n=75).

Optics EXPRESS

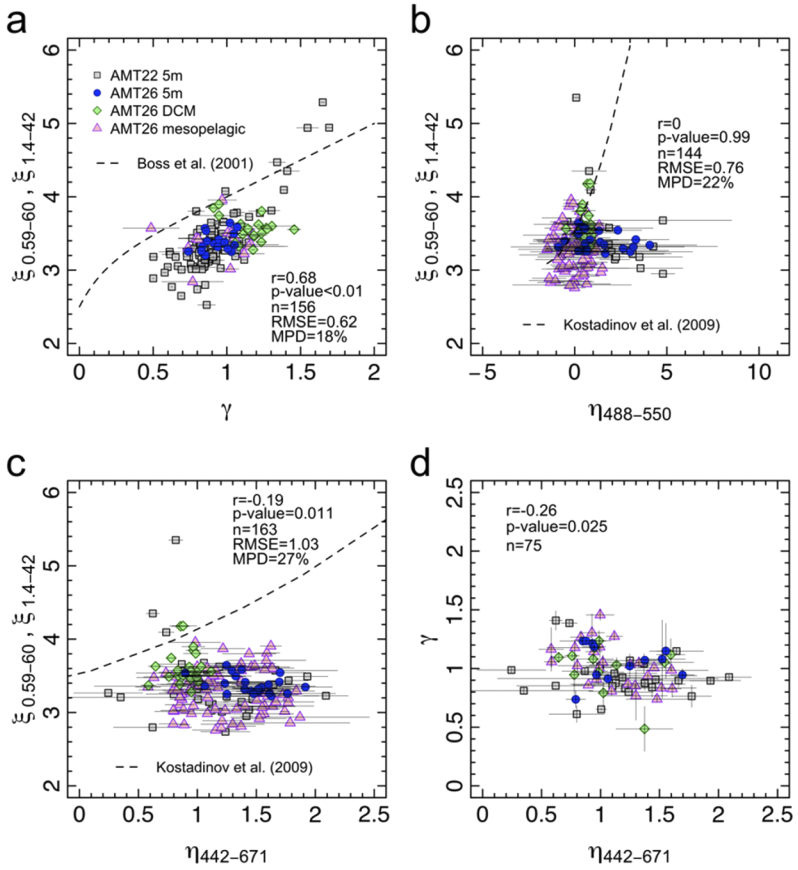


**Fig. 9.** Comparison between the slopes ξ computed over the entire measured size range and those derived from spectral optical measurements of beam attenuation ($c_p$) and particulate optical backscattering ($b_{bp}$) coefficients: (a) γ; (b) $\eta_{488-550}$; and (c) $\eta_{442-671}$; Error bars (black horizontal lines within each point) represent the standard deviation. Dashed lines represent previously published bio-optical models. Please note that previous models are limited to the range of γ and η values found in those studies. In panel (b), $\eta_{488-550}$ <-1.5 and >5 have been disregarded. Statistics for linear fits, RMSE and MPD values are shown. (d) Relationship between γ and $\eta_{442-671}$. Error bars (black lines within each point) represent the standard deviation. Statistics for linear fits are shown.

## 4. Discussion

Previous experimental studies have used the spectral properties of particulate beam attenuation ($c_p$) and optical backscattering ($b_{bp}$) coefficients to infer particle size distributions (PSDs) in the oceans. Good performance in retrieving PSD using both $c_p$ and $b_{bp}$ was observed in coastal waters, where minerals and lithogenic material are abundant, and for populations of particles with sizes spanning over several orders of magnitudes [9,13,40]. In open-ocean waters, PSDs were also modelled from spectral $b_{bp}$ measurements, though with high uncertainties [11]. Our results show that spectral $c_p$ is an optical proxy of PSDs only when a wide trophic range of Atlantic open-ocean waters is considered. In contrast, spectral $b_{bp}$ properties of marine particles were not related to co-located PSDs across the same trophic range and for the most oligotrophic waters of the Atlantic Ocean, between September and November (Fig. 9). Our results confirm findings for

Optics EXPRESS

other regions of the global ocean [15,33], and suggest prudence in using the spectral slope of $b_{bp}$ to infer the slope of open-ocean PSDs.

Theory [8] predicts steeper spectral slopes for both $c_p$ and $b_{bp}$ as the mean particle size decreases. The $\eta$ values measured by the HydroScat-6P during the AMT field expeditions were consistent with studies using different instruments [26], except for a few samples, and varied with seawater turbidity (Supplement 1, Fig. S5) as previously observed [33]. The lack of correlation observed between $\eta$ and $\gamma$ thus implies that these spectral optical scattering properties were driven by different factors. In an attempt to identify these factors, we differentiated between particles and phytoplankton, investigated the effects of light absorption, and analyzed their relationships with $\eta$ and $\gamma$ in our dataset.

At the surface and at the DCM, $\gamma$ was related to the abundance and fractions of particles larger than 1.4 µm (Fig. 10(a); Supplement 1, Table S2), while no or weakly-significant relationships were observed between $\gamma$ and the abundances of submicron particles (Supplement 1, Table S2). The variability of $\gamma$ was also significantly associated with the ratio of pico- to nano-eukaryotic phytoplankton (Fig. 10(b)), regardless of the varying relative contributions of phytoplankton and detritus between particle populations at the surface and at the DCM (Fig. 6). $\gamma$ was thus related to eukaryotic phytoplankton abundance and size distribution in our dataset.

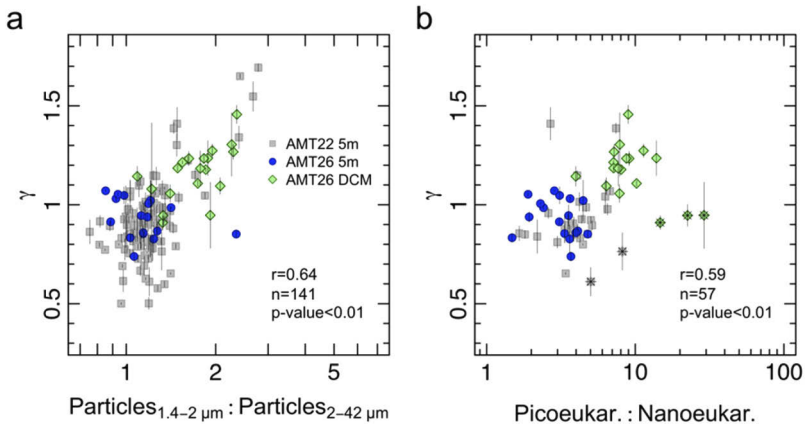


**Fig. 10.** Relationships between the slope $\gamma$ of the particulate beam attenuation coefficient ($c_p$), and: (a) ratios of the concentrations of particles with diameters between 1.4 and 2 µm to particles with diameters between 2 and 42 µm (from the Coulter Counter); (b) ratios of cellular abundances of pico-eukaryotes to nano-eukaryotes (from flow cytometry). Statistics for linear fits on the log-transformed particle and phytoplankton concentrations are shown (see Supplement 1, Table S2). Error bars (black vertical lines within each point) represent the standard deviation. In panel (b), statistics rely on all samples but stars (as they followed a different trend with statistics r=0.96, p-value<0.01, n=5). These starred DCM samples have been collected at equatorial latitudes.

The slope of $b_{bp}$ computed using measurements between 442 and 671 nm ($\eta_{442-671}$) also varied with phytoplankton abundances, when data at the DCM and surface were combined. $\eta_{442-671}$ was best correlated with the ratio between the abundances of cyanobacteria and eukaryotic phytoplankton across the upper Atlantic Ocean, even though this relationship was noisy (r=0.54, p-value<0.01, n=76; Fig. 11; Supplement 1, Table S3). Interestingly, the relationships between $\eta_{442-671}$ and the entire pool of particles (i.e., including detrital matter) were weaker than when only living eukaryotic phytoplankton was considered (Supplement 1, Table S3). Such weak relationships were consistent with the lack of correlation between $\eta_{442-671}$ and $\xi$ in Fig. 9. Moreover, we found that $\eta_{442-671}$ was not correlated with the abundance of all prokaryotes

Optics EXPRESS

(Supplement 1, Table S3). These results thus support previous findings that reinforce the role of phytoplankton as a driver of the $b_{bp}$ variability in the productive zone of open-ocean waters [14,20,41–43].

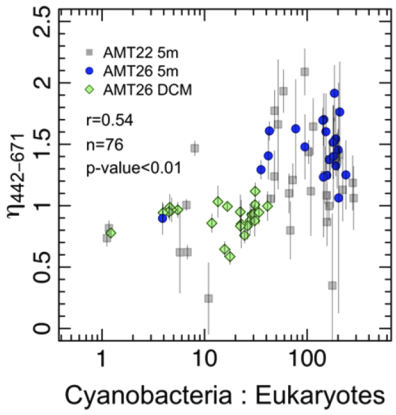


**Fig. 11.** The slope $\eta_{442-671}$ of the particulate optical backscattering coefficient ($b_{bp}$) as a function of the ratio of the concentrations of cyanobacteria and eukaryotic phytoplankton as measured by flow cytometry. Error bars (black vertical lines within each point) represent the standard deviation. Statistics for linear fits on the log-transformed ratios are shown (see Supplement 1, Table S3).

In the mesopelagic region of the Atlantic Ocean, $\eta_{442-671}$ roughly decreased with increasing concentrations of particles >1.14 µm (r=-0.25, p-value=0.02, n=86; Supplement 1, Table S4), and generally increased as a function of the ratio of small-to-large particles (r=0.27, p-value<0.01, n=86; Supplement 1, Fig. S7 and Table S4). For these samples, no significant relationships were observed with concentrations of particles <1.14 µm, phytoplankton and prokaryotes (Supplement 1, Table S4). Similar conclusions could not be drawn for $\gamma$ because the number of coincident measurements of spectral $c_p$ coefficients and flow cytometry was limited for that region of the ocean (n<15; Supplement 1, Table S5). The high relevance of detrital particles >1.14 µm for $\eta_{442-671}$ might be linked to differences in the nature of mesopelagic and upper-ocean particles. Indeed, as suggested by Organelli et al. [20], particles in the mesopelagic zone of the Atlantic Ocean may be made of harder material, or represent denser and more structurally complex and large aggregates, than for phytoplankton and detrital particles higher in the water column.

We found that $\eta$ was not a good proxy of marine particle size when it was computed over narrow spectral ranges. We analyzed the correlations between particle abundances and characteristics and $\eta$ computed between the wavelengths 488 and 550 nm, $\eta_{488-550}$, both in the upper ocean and in the mesopelagic zone. $\eta_{488-550}$ was not dependent on the concentration of particles of different sizes and nature (Supplement 1, Tables S6 and S7). Low correlations were only found between $\eta_{488-550}$, the abundance of particles > 1.14 µm, eukaryotes and the ratio of prokaryotes to eukaryotic phytoplankton in the upper ocean (Supplement 1, Table S6). These low correlations may be a consequence of the uncertainty associated with the $b_{bp}$ measurements at those wavelengths [44]. Indeed, $\eta_{488-550}$ was calculated using two relatively close bands that are characterized by uncertainties up to 40% in such waters [14,26] yielding a very large spectral variability in $b_{bp}$ (Fig. 8). Hence, we recommend that the spectral slope of $b_{bp}$ should be computed using data covering a wide spectral range.

The spectral slope of optical backscattering, $\eta$, was affected by the light absorption of the optically significant substances in water (Fig. 12). The slope $\eta_{442-671}$ decreased significantly as a function of the total light absorption ($a_{tot}$; Fig. 12(a)), but this relationship was not driven

Optics EXPRESS

by the light absorption of the colored dissolved organic matter ($a_{CDOM}$; r=-0.47, p-value<0.01, n=30), nor by the relative contribution of the light absorption by seawater ($a_w$) to $a_{tot}$ (r=0.37, p-value=0.02, n=41). The slope $\eta_{442-671}$ decreased as a function of the particulate light absorption coefficients ($a_p$) at 488 nm, though two different trends between particles from the mesopelagic region (r=-0.82, p-value<0.01, n=14) and those at the surface and at the DCM (r=-0.54, p-value<0.01, n=52) were observed (Fig. 12(b)). In contrast to $\eta_{442-671}$, $\gamma$ was less correlated with $a_{tot}$ (r=0.32, p-value=0.04, n=42) and $a_p(488)$ when AMT22 and AMT26 data were combined (r=0.36, p-value<0.01, n=69). Thus, we experimentally confirmed that spectral $c_p$ coefficients are more robust to variations in light absorption than spectral $b_{bp}$ [45]. In our samples at 5 m and at the DCM, the strong dependence of $\eta_{442-671}$ on $a_p$ could be the consequence of algal pigment absorption that depressed $b_{bp}$ in the blue as previously observed with algal culture experiments and in natural waters [45,46]. This effect is dependent on the relative size of the particles with respect to the wavelength, and on the real and imaginary refractive indices of the particles [47]. It is therefore expected to be larger with increasing size, because particles may contain more absorbing substances that reduce the backscattered light. Indeed, at 5 m and at the DCM, we found that $a_p(488)$ significantly increased with the concentration of eukaryotic phytoplankton ($\log_{10}(a_p(488)) = 0.61(\pm0.05)*\log_{10}(\text{Eukaryotes})-7.86(\pm0.51)$, r=0.83, p-value<0.01, n=62; Fig. 12(c)), which contains higher per-cell chlorophyll-*a* and other pigment concentrations than cyanobacteria [22]. The same $a_p(488)$ values decreased with increasing ratios of cyanobacteria to eukaryotic phytoplankton abundances (r=-0.69, p-value<0.01, n=62; Supplement 1, Fig. S8) but a poor correlation was observed with the concentration of cyanobacteria only (Fig. 12(d)). These findings thus suggested that the significant but noisy correlation observed between $\eta_{442-671}$ and the ratio of cyanobacteria to eukaryotic phytoplankton (Fig. 11; Supplement 1, Table S3) was likely a secondary consequence of the strong correlation observed between eukaryotic phytoplankton abundances and $a_p(488)$ (Fig. 12(c); Supplement 1, Fig. S8).

However, the $b_{bp}$ data acquired by the HydroScat-6P in this study were not corrected for light attenuation and absorption as the impact of the so called σ-correction on $b_{bp}$ coefficients was found to be negligible (Supplement 1, Table S1) [32]. For the sake of completeness, we also assessed the impact of the σ-correction on the values of $\eta_{442-671}$. The σ-correction was small and increased $\eta_{442-671}$ systematically (y=1.02x+0.07, $r^2$=0.99, p-value<0.01, n=133; where y and x are the values of $\eta_{442-671}$ after and before σ-correction, respectively; Supplement 1, Fig. S9) with RMSE and MPD equal to 0.09 and 7%, respectively. This sensitivity analysis helped also confirming that the impact of light absorption to spectral $b_{bp}$ coefficients is intrinsic in the $b_{bp}$ measurements [45], and further prevents one from using spectral $b_{bp}$ properties to study open-ocean PSD dynamics.

When using optical measurements to estimate PSDs, another important limitation comes from the choice of the slope of a power-law fit as single predictor of particle size (i.e., ξ). This choice is convenient for bio-optical modelling but it represents an oversimplification of reality [36,48–51]. Our data from AMT26 clearly showed that a single slope of PSD cannot describe the large variability of marine particle sizes and concentrations encountered across the upper 500 m of the Atlantic Ocean (Fig. 4). The size distribution of submicron particles was drastically different from, and uncorrelated to, that of particles with diameters >1 µm (Fig. 5; Supplement 1, Fig. S4). Our measurements showed peaks that were likely associated with prokaryotic populations below and around 0.6 µm that, unfortunately, could not be fully resolved because of the Coulter Counter's detection limits. The occurrence of such peaks should discourage the use of ξ values that describe PSDs increasing continuously as a function of decreasing particle diameters, as well as the use of the $\xi_{0.59-1.14}$ values for submicron particles reported in this study. In addition, ξ cannot reproduce any peak due to specific particle populations such those observed for particles >1 µm (Fig. 4). These peaks included picoeukaryotes and nano-phytoplankton and

Optics EXPRESS

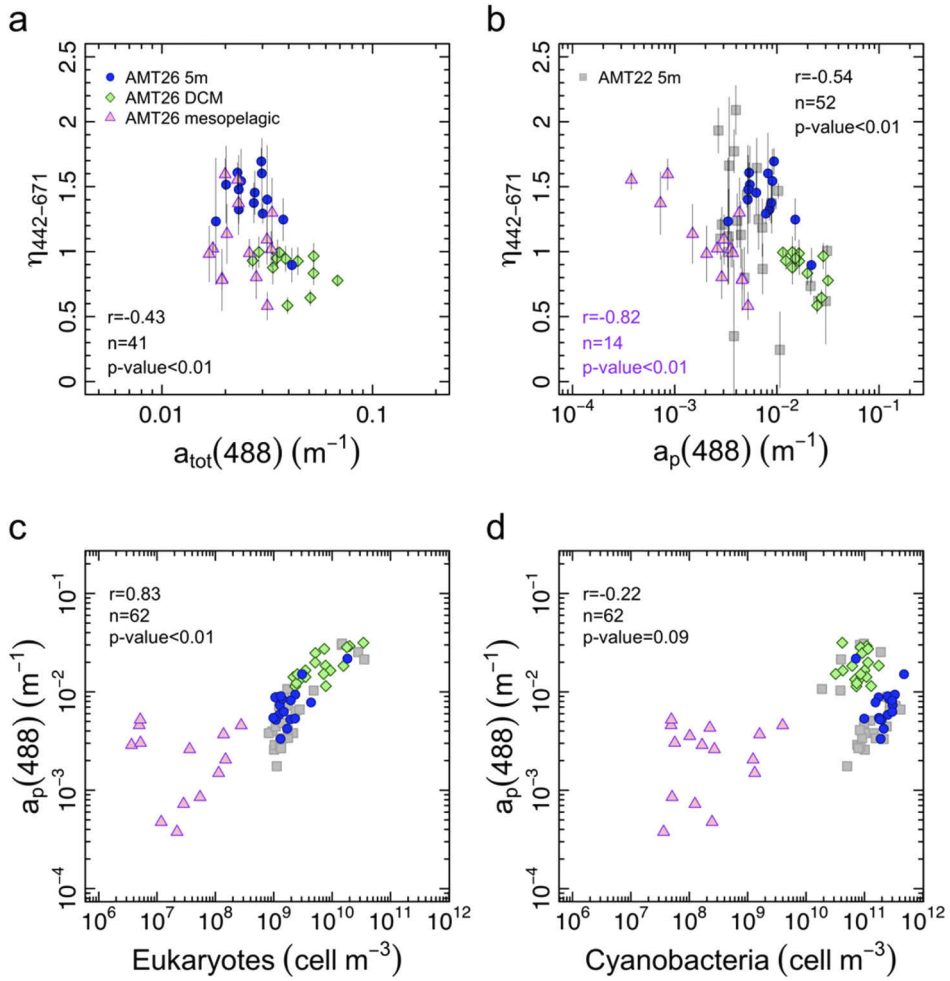


**Fig. 12.** Relationships between the slope $\eta_{442-671}$ of the particulate optical backscattering coefficient ($b_{bp}$) as a function of (a) the total light absorption coefficients ($a_{tot}$) at 488 nm; and (b) the particulate light absorption coefficients ($a_p$) at 488 nm. Error bars (black vertical lines within each point) represent the standard deviation. Statistics for linear fits on the log-transformed light absorption coefficients are shown. In plot (b), statistics colored in black refer to samples collected at 5 m and at the level of the DCM while those colored in purple refer to mesopelagic samples only. Relationships between the particulate light absorption coefficients ($a_p$) at 488 nm as a function of (c) the concentration of eukaryotic phytoplankton; and (d) the concentration of cyanobacteria. Statistics for linear fits on log-transformed quantities are shown and refer only to samples collected at 5 m and at the level of the DCM.

significantly influenced the particle area concentration (Fig. 3), which is directly related to the optical scattering properties of marine particles [13,52].

## 5. Conclusions

We investigated the particulate spectral scattering properties ($c_p$ and $b_{bp}$) as proxies of marine particle size in the upper 500 m of the Atlantic Ocean, across various trophic regimes including mid-ocean gyres. We analyzed the relationships linking $\xi$ to $\gamma$ and $\eta$, and their potential drivers

Optics EXPRESS

using an unprecedented dataset of co-located spectral $c_p$ and $b_{bp}$ coefficients, particle size distributions from a Coulter Counter, phytoplankton abundancies from flow cytometry, and light absorption measurements. The main findings of this analysis are:

a. The slope of $b_{bp}$ ($\eta$) was not a good proxy of the slope of the PSD ($\xi$) in the upper 500 m of the Atlantic Ocean, while the slope of $c_p$ ($\gamma$) was related to $\xi$ only over a wide range of trophic conditions;

b. $\gamma$ was related to the ratio of the abundances of pico- and nano-eukaryotic phytoplankton, and was robust to variations in light absorption;

c. $\eta$ values were significantly related to the light absorption by particles in the upper ocean and in the mesopelagic zone;

d. $\eta$ was also related to the ratio of the abundances of cyanobacteria and eukaryotic phytoplankton, although this relationship was likely due to the correlation between particle light absorption and the concentration of eukaryotic phytoplankton;

e. $\eta$ values computed over a narrow spectral range using a HydroScat-6P offered little information on marine particles.

To explore the dynamics of particles in the open-ocean waters of the Atlantic Ocean, the spectral slopes of $c_p$ and $b_{bp}$ thus showed some limitations, even though $\gamma$ was to first order related to the slope of the PSD and eukaryotic phytoplankton.

## Funding

H2020 Marie Skłodowska-Curie Actions (706781); Natural Environment Research Council (NE/R015953/1, NER/0/5/2001/00680); European Space Agency (4000125730/18/NL/FF/gp, ESRIN/RFQ/3-14457/16/I-BG); National Aeronautics and Space Administration (NNX10AT70G).

## Acknowledgments

This study is a contribution to the REOPTIMIZE – REmineralisation, OPTIcs and Marine partIcle siZE project which was supported by the European Union's Horizon 2020 research and innovation program under the Marie Skłodowska-Curie actions. This study was supported by the European Space Agency contract: Copernicus Sentinel Atlantic Meridional Transect Fiducial Reference Measurements Campaign (AMT4SentinelFRM). This study contains data supplied by the Natural Environmental Research Council as provided by the British Oceanographic Data Centre and the Atlantic Meridional Transect Consortium. The Atlantic Meridional Transect is funded by the UK Natural Environment Research Council through its National Capability Long-term Single Centre Science Programme, Climate Linked Atlantic Sector Science. This study contributes to the international IMBeR project and is contribution number 338 of the AMT program. We thank the captains, officers and crew of the RRS James Cook (UK National Oceanography Centre) and the RRS James Clark Ross (British Antarctic Survey) for helping in data collection during AMT22 and AMT26 field expeditions. We thank Kristen Reifel and Virginie van Dongen-Vogels for helping in AMT22 ship's underway data collection, Urania Christaki and Mikhail Zubkov for AMT22 flow cytometry measurements, and Marco Bellacicco for useful comments.

## Disclosures

The authors declare no conflicts of interest.

Optics EXPRESS

See Supplement 1 for supporting content.

## Data Availability

Particle size distribution data collected on the AMT26 cruise are available at https://doi.org/10.5285/79103bda-8913-39f3-e053-6c86abc0567a. All other data are freely available at https://www.bodc.ac.uk/projects/uk/amt/.

## References


1. P. G. Falkowski, "Biogeochemical controls and feedbacks on ocean primary production," Science **281**(5374), 200–206 (1998).
2. T. W. Trull, S. G. Bray, K. O. Buesseler, C. H. Lamborg, S. Manganini, C. Moy, and J. Valdes, "In situ measurement of mesopelagic particle sinking rates and the control of carbon transfer to the ocean interior during the Vertical Flux in the Global Ocean (VERTIGO) voyages in the North Pacific," Deep Sea Res., Part II **55**(14-15), 1684–1695 (2008).
3. P. G. Falkowski, "Do tiny floating microorganisms in the ocean's surface waters play a massive role in controlling the global climate?" Nature **483**(7387), S17–S20 (2012).
4. L. Stemmann and E. Boss, "Plankton and particle size and packaging: from determining optical properties to driving the biological pump," Annu. Rev. Mar. Sci. **4**(1), 263–290 (2012).
5. F. Lombard, E. Boss, A. M. Waite, M. Vogt, J. Uitz, L. Stemmann, H. M. Sosik, J. Schulz, J.-B. Romagnan, M. Picheral, J. Pearlman, M. D. Ohman, B. Niehoff, K. O. Möller, P. Miloslavich, A. Lara-Lpez, R. Kudela, R. M. Lopes, R. Kiko, L. Karp-Boss, J. S. Jaffe, M. H. Iversen, J.-O. Irisson, K. Fennel, H. Hauss, L. Guidi, G. Gorsky, S. L. C. Giering, P. Gaube, S. Gallager, G. Dubelaar, R. K. Cowen, F. Carlotti, C. Briseño-Avena, L. Berline, K. Benoit-Bird, N. Bax, S. Batten, S. D. Ayata, L. F. Artigas, and W. Appeltans, "Globally consistent quantitative observations of planktonic ecosystems," Front. Mar. Sci. **6**, 196 (2019).
6. R. W. Sheldon and T. R. Parsons, *A Practical Manual on the Use of the Coulter Counter in Marine Research* (Coulter Electronics Sales Company, 1967).
7. F. Partensky, J. Blanchot, F. Lantoine, J. Neveux, and D. Marie, "Vertical structure of picophytoplankton at different trophic sites of the tropical northeastern Atlantic Ocean," Deep Sea Res., Part I **43**(8), 1191–1213 (1996).
8. A. Morel, *Diffusion de La Lumière Par Les Eaux de Mer. Résultats Experimentaux et Approche Théorique* AGARD Lecture Series No. 61 (NATO, 1973).
9. E. Boss, M. S. Twardowski, and S. Herring, "Shape of the particulate beam attenuation spectrum and its inversion to obtain the shape of the particulate size distribution," Appl. Opt. **40**(27), 4885–4893 (2001).
10. H. Loisel, J.-M. Nicolas, A. Sciandra, D. Stramski, and A. Poteau, "Spectral dependency of optical backscattering by marine particles from satellite remote sensing of the global ocean," J. Geophys. Res. **111**(C9), C09024 (2006).
11. T. S. Kostadinov, D. A. Siegel, and S. Maritorena, "Retrieval of the particle size distribution from satellite ocean color observations," J. Geophys. Res. **114**(C9), C09015 (2009).
12. R. A. Reynolds, D. Stramski, V. M. Wright, and S. B. Woźniak, "Measurements and characterization of particle size distributions in coastal waters," J. Geophys. Res. **115**(C8), C08024 (2010).
13. W. H. Slade and E. Boss, "Spectral attenuation and backscattering as indicators of average particle size," Appl. Opt. **54**(24), 7264–7277 (2015).
14. G. Dall'Olmo, T. K. Westberry, M. J. Behrenfeld, E. Boss, and W. H. Slade, "Significant contribution of large particles to optical backscattering in the open ocean," Biogeosciences **6**(6), 947–967 (2009).
15. E. Boss, N. Haëntjens, T. K. Westberry, L. Karp-Boss, and W. H. Slade, "Validation of the particle size distribution obtained with the laser in-situ scattering and transmission (LISST) meter in flow-through mode," Opt. Express **26**(9), 11125–11136 (2018).
16. D. Antoine, D. A. Siegel, T. Kostadinov, S. Maritorena, N. B. Nelson, B. Gentili, V. Vellucci, and N. Guillocheau, "Variability in optical particle backscattering in contrasting bio-optical oceanic regimes," Limnol. Oceanogr. **56**(3), 955–973 (2011).
17. K. Niewiadomska, H. Claustre, L. Prieur, and F. d'Ortenzio, "Submesoscale physical-biogeochemical coupling across the Ligurian current (northwestern Mediterranean) using a bio-optical glider," Limnol. Oceanogr. **53**(5part2), 2210–2225 (2008).
18. E. Organelli, M. Barbieux, H. Claustre, C. Schmechtig, A. Poteau, A. Bricaud, E. Boss, N. Briggs, G. Dall'Olmo, F. D'Ortenzio, E. Leymarie, A. Mangin, G. Obolensky, C. Penkerc'h, L. Prieur, C. Roesler, R. Serra, J. Uitz, and X. Xing, "Two databases derived from BGC-Argo float measurements for marine biogeochemical and bio-optical applications," Earth Syst. Sci. Data **9**(2), 861–880 (2017).
19. J. Pitarch, M. Bellacicco, E. Organelli, G. Volpe, S. Colella, V. Vellucci, and S. Marullo, "Retrieval of particulate backscattering using field and satellite radiometry: Assessment of the QAA algorithm," Remote Sens. **12**(1), 77 (2020).
20. E. Organelli, G. Dall'Olmo, R. J. W. Brewin, G. A. Tarran, E. Boss, and A. Bricaud, "The open-ocean missing backscattering is in the structural complexity of particles," Nat. Commun. **9**(1), 5439 (2018).

Optics EXPRESS


21. BIMP and ISO, *Guide to the Expression of Uncertainty in Measurement* (International Organization for Standardization, 1995).
22. E. Organelli, C. Nuccio, L. Lazzara, J. Uitz, A. Bricaud, and L. Massi, "On the discrimination of multiple phytoplankton groups from light absorption spectra of assemblages with mixed taxonomic composition and variable light conditions," Appl. Opt. **56**(14), 3952–3968 (2017).
23. G. A. Tarran, J. L. Heywood, and M. V. Zubkov, "Latitudinal changes in the standing stocks of nano- and picoeukaryotic phytoplankton in the Atlantic Ocean," Deep Sea Res., Part II **53**(14-16), 1516–1529 (2006).
24. J. L. Heywood, M. V. Zubkov, G. A. Tarran, B. M. Fuchs, and P. M. Holligan, "Prokaryoplankton standing stocks in oligotrophic gyre and equatorial provinces of the Atlantic Ocean: Evaluation of inter-annual variability," Deep Sea Res., Part II **53**(14-16), 1530–1547 (2006).
25. E. Boss, W. H. Slade, M. Behrenfeld, and G. Dall'Olmo, "Acceptance angle effects on the beam attenuation in the ocean," Opt. Express **17**(3), 1535–1550 (2009).
26. G. Dall'Olmo, E. Boss, M. J. Behrenfeld, and T. K. Westberry, "Particulate optical scattering coefficients along an Atlantic Meridional Transect," Opt. Express **20**(19), 21532–21551 (2012).
27. J. R. V. Zaneveld, J. C. Kitchen, and C. C. Moore, "Scattering error correction of reflecting-tube absorption meters," in J. S. Jaffe, ed., (1994), 44–55.
28. G. Dall'Olmo, R. J. W. Brewin, F. Nencioli, E. Organelli, I. Lefering, D. McKee, R. Röttgers, C. Mitchell, E. Boss, A. Bricaud, and G. Tilstone, "Determination of the absorption coefficient of chromophoric dissolved organic matter from underway spectrophotometry," Opt. Express **25**(24), A1079–A1095 (2017).
29. R. M. Pope and E. S. Fry, "Absorption spectrum (380–700 nm) of pure water II Integrating cavity measurements," Appl. Opt. **36**(33), 8710–8723 (1997).
30. X. Zhang, L. Hu, and M.-X. He, "Scattering by pure seawater: Effect of salinity," Opt. Express **17**(7), 5698–5710 (2009).
31. HOBILabs, *HydroScat-6P, Spectral Backscattering Sensor & Fluorometer* (HOBILabs, 2010).
32. D. Stramski, R. A. Reynolds, M. Babin, S. Kaczmarek, M. R. Lewis, R. Röttgers, A. Sciandra, M. Stramska, M. S. Twardowski, B. A. Franz, and H. Claustre, "Relationships between the surface concentration of particulate organic carbon and optical properties in the eastern South Pacific and eastern Atlantic Oceans," Biogeosciences **5**(1), 171–201 (2008).
33. R. A. Reynolds, D. Stramski, and G. Neukermans, "Optical backscattering by particles in Arctic seawater and relationships to particle mass concentration, size distribution, and bulk composition: Particle backscattering in Arctic seawater," Limnol. Oceanogr. **61**(5), 1869–1890 (2016).
34. J. W. Campbell, "The lognormal distribution as a model for bio-optical variability in the sea," J. Geophys. Res. **100**(C7), 13237–13254 (1995).
35. C. J. Buonassissi and H. M. Dierssen, "A regional comparison of particle size distributions and the power law approximation in oceanic and estuarine surface waters," J. Geophys. Res. **115**(C10), C10028 (2010).
36. H. Runyan, R. A. Reynolds, and D. Stramski, "Evaluation of particle size distribution metrics to estimate the relative contributions of different size fractions based on measurements in Arctic waters," J. Geophys. Res.: Oceans **125**(6), e2020JC016218 (2020).
37. C. Grob, O. Ulloa, H. Claustre, Y. Huot, G. Alarcón, and D. Marie, "Contribution of picoplankton to the total particulate organic carbon concentration in the eastern South Pacific," Biogeosciences **4**(5), 837–852 (2007).
38. F. Partensky, W. R. Hess, and D. Vaulot, "Prochlorococcus, a marine photosynthetic prokaryote of global significance," Microbiol. Mol. Biol. Rev. **63**(1), 106–127 (1999).
39. E. Boss, M. Picheral, T. Leeuw, A. Chase, E. Karsenti, G. Gorsky, L. Taylor, W. Slade, J. Ras, and H. Claustre, "The characteristics of particulate absorption, scattering and attenuation coefficients in the surface ocean; Contribution of the Tara Oceans expedition," Methods Oceanogr. **7**, 52–62 (2013).
40. S. B. Woźniak and D. Stramski, "Modeling the optical properties of mineral particles suspended in seawater and their influence on ocean reflectance and chlorophyll estimation from remote sensing algorithms," Appl. Opt. **43**(17), 3489–3503 (2004).
41. X. Zhang, L. Hu, Y. Xiong, Y. Huot, and D. Gray, "Experimental estimates of optical backscattering associated with submicron particles in clear oceanic waters," Geophys. Res. Lett. **47**(4), e2020GL087100 (2020).
42. C. Poulin, X. Zhang, P. Yang, and Y. Huot, "Diel variations of the attenuation, backscattering and absorption coefficients of four phytoplankton species and comparison with spherical, coated spherical and hexahedral particle optical models," J. Quant. Spectrosc. Radiat. Transfer **217**, 288–304 (2018).
43. L. Duforêt-Gaurier, D. Dessailly, W. Moutier, and H. Loisel, "Assessing the impact of a two-layered spherical geometry of phytoplankton cells on the bulk backscattering ratio of marine particulate matter," Appl. Sci. **8**(12), 2689 (2018).
44. D. McKee, M. Chami, I. Brown, V. S. Calzado, D. Doxaran, and A. Cunningham, "Role of measurement uncertainties in observed variability in the spectral backscattering ratio: A case study in mineral-rich coastal waters," Appl. Opt. **48**(24), 4663–4675 (2009).
45. A. Bricaud, A. Morel, and L. Prieur, "Optical efficiency factors of some phytoplankters," Limnol. Oceanogr. **28**(5), 816–832 (1983).
46. H. R. Gordon, M. R. Lewis, S. D. McLean, M. S. Twardowski, S. A. Freeman, K. J. Voss, and G. C. Boynton, "Spectra of particulate backscattering in natural waters," Opt. Express **17**(18), 16192–16208 (2009).

Optics EXPRESS

47. A. Bricaud and A. Morel, "Light attenuation and scattering by phytoplanktonic cells: A theoretical modeling," Appl. Opt. **25**(4), 571–580 (1986).
48. D. Risović, "Two-component model of sea particle size distribution," Deep Sea Res., Part I **40**(7), 1459–1473 (1993).
49. D. Risović, "Effect of suspended particulate-size distribution on the backscattering ratio in the remote sensing of seawater," Appl. Opt. **41**(33), 7092–7101 (2002).
50. M. Jonasz and G. Fournier, "Approximation of the size distribution of marine particles by a sum of log-normal functions," Limnol. Oceanogr. **41**(4), 744–754 (1996).
51. G. Fournier and G. Neukermans, "An analytical model for light backscattering by coccoliths and coccospheres of Emiliania huxleyi," Opt. Express **25**(13), 14996–15009 (2017).
52. A. Morel and A. Bricaud, "Inherent optical properties of algal cells including picoplankton: Theoretical and experimental results," Can. Bull. Fish. Aquat. Sci. **214**, 521–559 (1986).

Supplemental Document

Optics EXPRESS

# Drivers of spectral optical scattering by particles in the upper 500 m of the Atlantic Ocean: supplement

EMANUELE ORGANELLI,[1,2,*] GIORGIO DALL'OLMO,[1,3] ROBERT J. W. BREWIN,[1,4] FRANCESCO NENCIOLI,[1] AND GLEN A. TARRAN[1]

[1] *Plymouth Marine Laboratory, Prospect Place, The Hoe, PL1 3DH Plymouth, UK*
[2] *National Research Council (CNR), Institute of Marine Sciences (ISMAR), Via Fosso del Cavaliere 100, 00133 Rome, Italy*
[3] *National Centre for Earth Observation, Plymouth Marine Laboratory, Prospect Place, The Hoe, PL1 3DH Plymouth, UK*
[4] *University of Exeter, College of Life and Environmental Sciences, Penryn Campus, Cornwall TR10 9FE, UK*
[*] *emanuele.organelli@cnr.it*



Supplement DOI: https://doi.org/10.6084/m9.figshare.13096139

Parent Article DOI: https://doi.org/10.1364/OE.408439

# Drivers of spectral optical scattering by particles in the upper 500 m of the Atlantic Ocean: supplemental document

This document contains supplementary figures and tables which have been ordered as they appear in the main manuscript.

**Table S1. Mean (plus standard deviation, sd) $K_{bb}$ correction factors estimated for each band acquired by the HydroScat-6P on AMT26, and magnitude of the σ-correction with respect to uncorrected optical backscattering coefficients (i.e, $b_{bp}$). RMSE is the root mean square error.**

| Band | $K_{bb}$ | | $b_{bp}$ | | | | |
|---|---|---|---|---|---|---|---|
| | Mean±sd ($m^{-1}$) | n | Mean±sd (%) | Min (%) | Max (%) | RMSE ($m^{-1}$) | n |
| **442**[a] | 0.050±0.025 | 43 | 4.16±1.18 | 1.80 | 6.10 | $2.53*10^{-5}$ | 134 |
| **488** | 0.036±0.023 | 43 | 3.25±1.20 | 1.19 | 6.73 | $1.27*10^{-5}$ | 134 |
| **550**[b] | 0.023±0.016 | 43 | 1.44±0.42 | 0.61 | 2.51 | $5.55*10^{-6}$ | 134 |
| **620**[c] | 0.018±0.014 | 43 | 0.88±0.27 | 0.41 | 1.62 | $2.76*10^{-6}$ | 134 |
| **671**[d] | 0.018±0.016 | 43 | 0.67±0.16 | 0.37 | 1.04 | $2.60*10^{-6}$ | 134 |

[a] computed using ac-9 and $a_{CDOM}$ measurements at 440 nm
[b] computed using ac-9 and $a_{CDOM}$ measurements at 554 nm
[c] computed using ac-9 and $a_{CDOM}$ measurements at 650 nm
[d] computed using ac-9 and $a_{CDOM}$ measurements at 676 nm

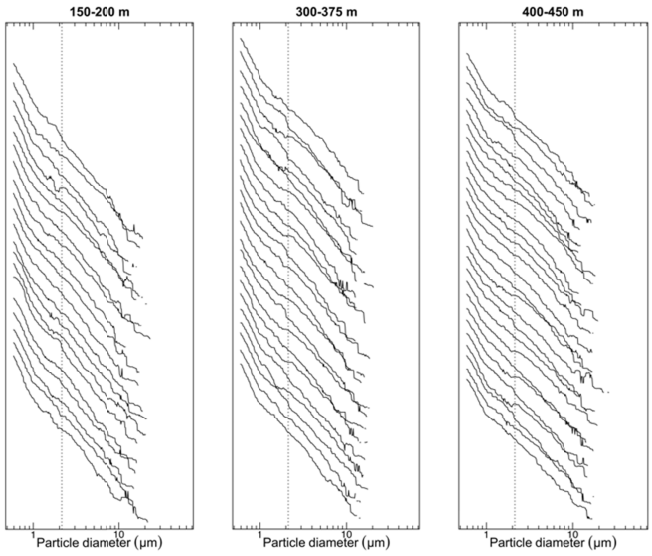


**Fig. S1.** Particle size distributions (PSDs) collected during the AMT26 cruise at the following depths: 150-200 m, 300-375 m and 400-450 m. In each panel, PSDs are shown in logarithmic scale. To improve visualization, PSDs have been spaced, and smoothed with a moving-median filter (fifteen point window). Dashed vertical lines indicated lower and upper limits of the size bin at which the PSDs acquired with the Coulter Counter's tube apertures of 20 µm and 100 µm diameters were merged.

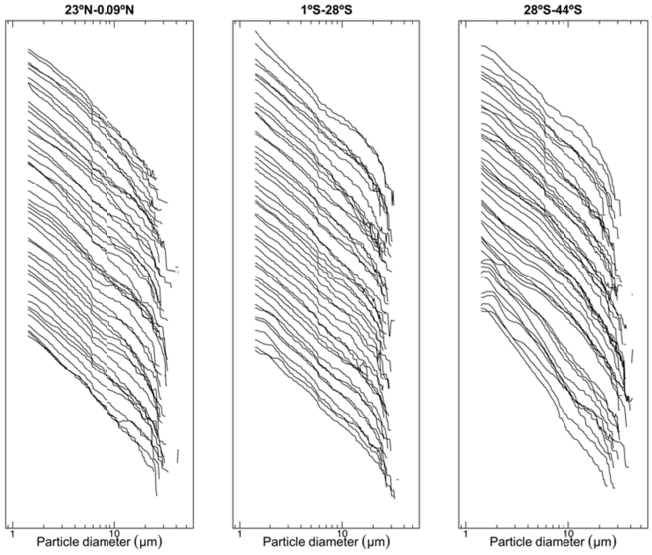


**Fig. S2.** Particle size distributions (PSDs) collected during the AMT22 cruise at 5 m depth, grouped according to the latitude. In each panel, PSDs are shown in logarithmic scale. To improve visualization, PSDs have been spaced, and smoothed with a moving-median filter (fifteen point window).

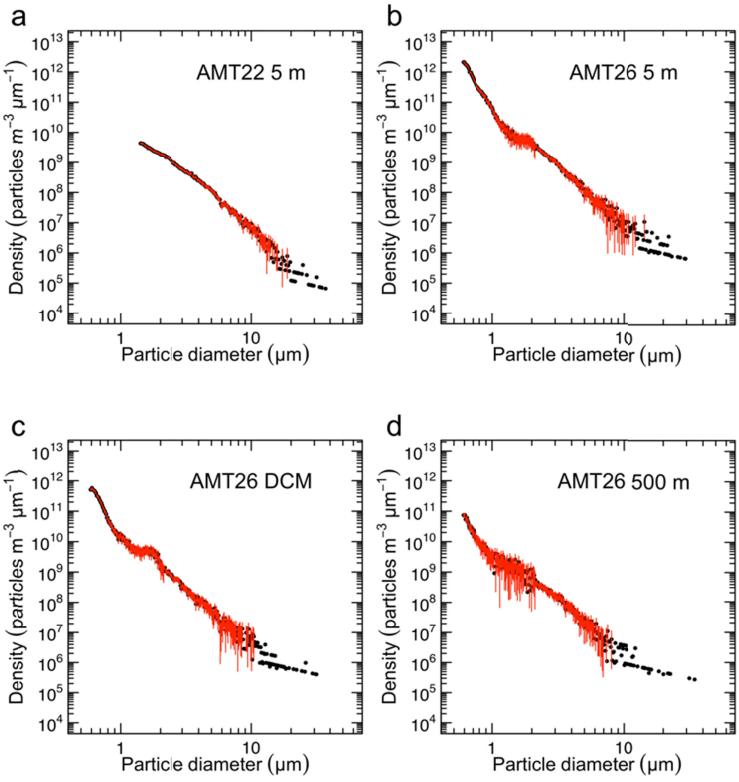


**Fig. S3.** Examples of particle size distributions collected at various depths during the AMT22 and AMT26 cruises, as a function of the particle diameter. Error bars represent the combined uncertainty (95% confidence intervals) as propagated from the summation of multiple particle size distribution measurements (see methods).

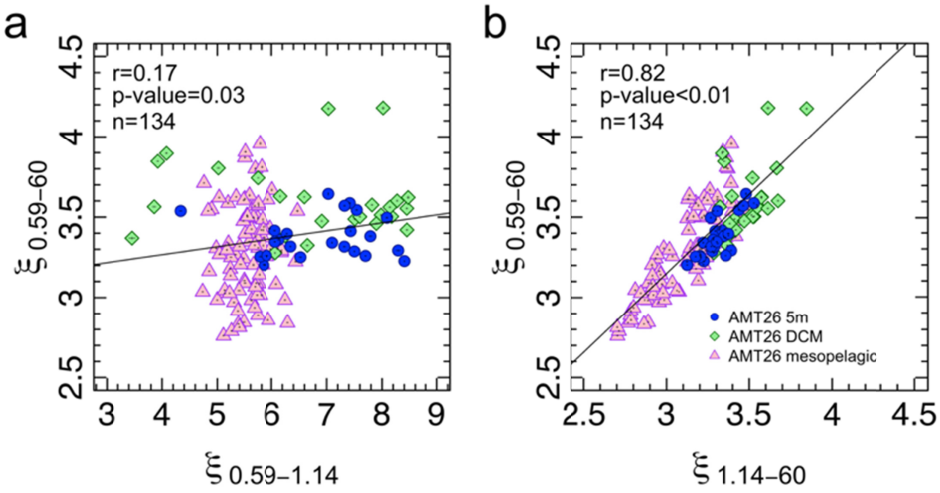


**Fig. S4.** Comparison between the slopes ξ of particle size distributions computed for particle diameters between 0.59 and 60 µm ($\xi_{0.59\text{-}60}$) and: (a) ξ computed for particle diameters between 0.59 and 1.14 µm ($\xi_{0.59\text{-}1.14}$); (b) ξ computed for particle diameters between 1.14 µm and 60 µm ($\xi_{1.14\text{-}60}$). Horizontal and vertical bars indicate the error associated to each ξ as derived from the power law fit and Monte Carlo simulations (see methods). Solid lines are the linear fits and statistics are shown.

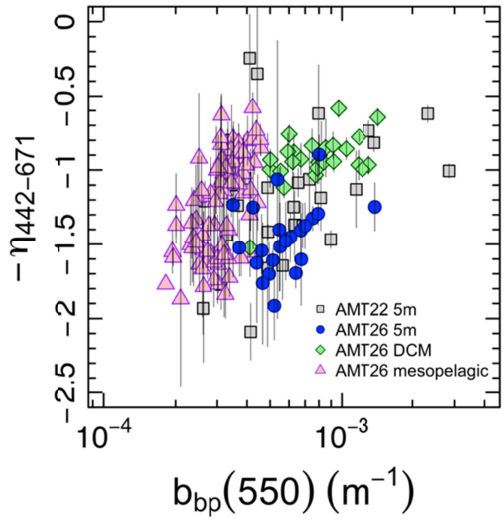


**Fig. S5.** Relationship between the slope $\eta_{442\text{-}671}$ of the particulate optical backscattering coefficient ($b_{bp}$) and $b_{bp}(550)$ for different cruises and depths. Error bars (black vertical lines within each point) represent the standard deviation.

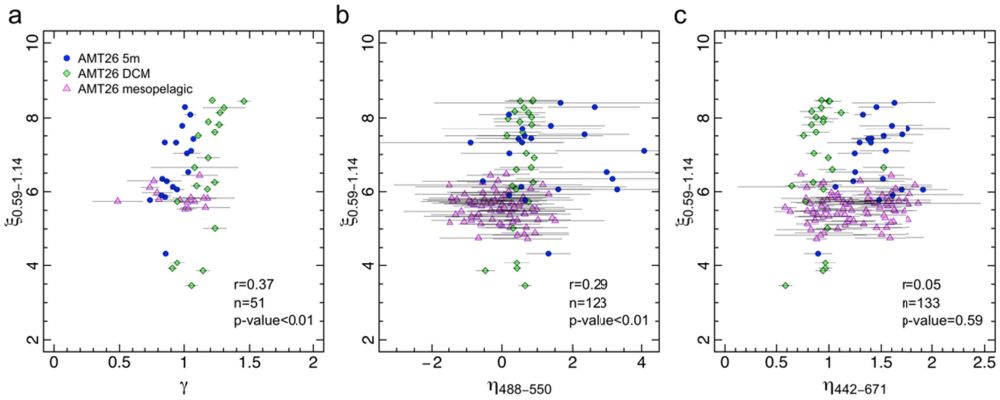


**Fig. S6.** Comparison between the slopes of particle size distributions computed for particle diameters between 0.59 and 1.14 µm, $\xi_{0.59\text{-}1.14}$, and: (a) the slope of the particulate beam attenuation coefficient ($c_p$), $\gamma$; (b) the slope of the particulate optical backscattering coefficient ($b_{bp}$) between 488 and 550 nm, $\eta_{488\text{-}550}$; and (c) the slope of the particulate optical backscattering coefficient ($b_{bp}$) between 442 and 671 nm, $\eta_{442\text{-}671}$. Error bars (black horizontal lines within each point) represent the standard deviation. In panel (b), $\eta_{488\text{-}550}$ <-1.5 and >5 have been disregarded. Statistics for linear fits are shown.

**Table S2. Correlation coefficient (r), number of points (n) and p-value for linear fits between the slope of the particulate beam attenuation coefficient ($c_p$) and various log-transformed particle concentrations and ratios. Prokaryotes are defined as the sum of cyanobacteria and heterotrophic bacteria. Only samples collected at 5 m and the depth of the deep chlorophyll maximum are used. $^{**}$highly significant; $^{*}$significant; $^{ns}$not significant.**

| Concentrations | r | n | p-value | Cruise |
|---|---|---|---|---|
| Particles 0.6-60 µm | 0.19 | 36 | $0.28^{ns}$ | AMT26 |
| Particles 0.6-1.14 µm | 0.22 | 36 | $0.21^{ns}$ | AMT26 |
| Particles 1.14-60 µm | -0.14 | 36 | $0.40^{ns}$ | AMT26 |
| Particles 1.4-42 µm | 0.25 | 141 | $<0.01^{**}$ | AMT22, AMT26 |
| Prokaryotes | -0.15 | 60 | $0.23^{ns}$ | AMT22, AMT26 |
| Cyanobacteria | -0.10 | 62 | $0.44^{ns}$ | AMT22, AMT26 |
| Eukaryotes | 0.34 | 62 | $<0.01^{**}$ | AMT22, AMT26 |

| Ratios | r | n | p-value | Cruise |
|---|---|---|---|---|
| Particles 0.6-1.14 µm : Particles 1.14-60 µm | 0.38 | 36 | $0.02^{*}$ | AMT26 |
| Prokaryotes : Eukaryotes | -0.36 | 60 | $<0.01^{**}$ | AMT22, AMT26 |
| Cyanobacteria : Eukaryotes | -0.29 | 62 | $0.02^{*}$ | AMT22, AMT26 |
| Particles 1.4-2 µm : Particles 2-42 µm | 0.64 | 141 | $<0.01^{**}$ | AMT22, AMT26 |
| Pico-eukaryotes : Nano-eukaryotes | 0.38 | 62 | $<0.01^{**}$ | AMT22, AMT26 |
| | $(0.59)^{a}$ | $(57)^{a}$ | $(<0.01^{**})^{a}$ | |

[a]See Figure 10b in the main manuscript for DCM samples excluded from the analysis.

**Table S3. Correlation coefficient (r), number of points (n) and p-value for linear fits between the slope of the particulate optical backscattering coefficient ($b_{bp}$) between 442 and 671 nm and various log-transformed particle concentrations and ratios. Prokaryotes are defined as the sum of cyanobacteria and heterotrophic bacteria. Only samples collected at 5 m and the depth of the deep chlorophyll maximum are used. $^{**}$highly significant; $^{*}$significant; $^{ns}$not significant.**

| Concentrations | r | n | p-value | Cruise |
|---|---|---|---|---|
| Particles 0.6-60 µm | -0.42 | 47 | $<0.01^{**}$ | AMT26 |
| Particles 0.6-1.14 µm | -0.40 | 47 | $<0.01^{**}$ | AMT26 |
| Particles 1.14-60 µm | -0.40 | 77 | $<0.01^{**}$ | AMT22, AMT26 |
| Prokaryotes | -0.16 | 73 | $0.18^{ns}$ | AMT22, AMT26 |
| Cyanobacteria | 0.38 | 76 | $<0.01^{**}$ | AMT22, AMT26 |
| Eukaryotes | -0.51 | 76 | $<0.01^{**}$ | AMT22, AMT26 |

| Ratios | r | n | p-value | Cruise |
|---|---|---|---|---|
| Particles 0.6-1.14 µm : Particles 1.14-60 µm | 0.05 | 47 | $0.75^{ns}$ | AMT26 |
| Prokaryotes : Eukaryotes | 0.46 | 73 | $<0.01^{**}$ | AMT22, AMT26 |
| Cyanobacteria : Eukaryotes | 0.54 | 76 | $<0.01^{**}$ | AMT22, AMT26 |

**Table S4. Correlation coefficient (r), number of points (n) and p-value for linear fits between the slope of the particulate optical backscattering coefficient ($b_{bp}$) between 442 and 671 nm and various log-transformed particle concentrations and ratios. Prokaryotes are defined as the sum of cyanobacteria and heterotrophic bacteria. Only samples collected in the mesopelagic region are used. $^{**}$highly significant; $^{*}$significant; $^{ns}$not significant.**

| Concentrations | r | n | p-value | Cruise |
|---|---|---|---|---|
| Particles 0.6-60 µm | 0.03 | 86 | $0.75^{ns}$ | AMT26 |
| Particles 0.6-1.14 µm | 0.07 | 86 | $0.51^{ns}$ | AMT26 |
| Particles 1.14-60 µm | -0.25 | 86 | $0.02^{*}$ | AMT26 |
| Prokaryotes | 0.27 | 20 | $0.25^{ns}$ | AMT26 |
| Cyanobacteria | -0.39 | 20 | $0.09^{ns}$ | AMT26 |
| Eukaryotes | 0.07 | 18 | $0.79^{ns}$ | AMT26 |

| Ratios | r | n | p-value | Cruise |
|---|---|---|---|---|
| Particles 0.6-1.14 µm : Particles 1.14-60 µm | 0.27 | 86 | $0.01^{*}$ | AMT26 |
| Prokaryotes : Eukaryotes | -0.03 | 18 | $0.90^{ns}$ | AMT26 |
| Cyanobacteria : Eukaryotes | -0.81 | 18 | $<0.01^{**}$ | AMT26 |

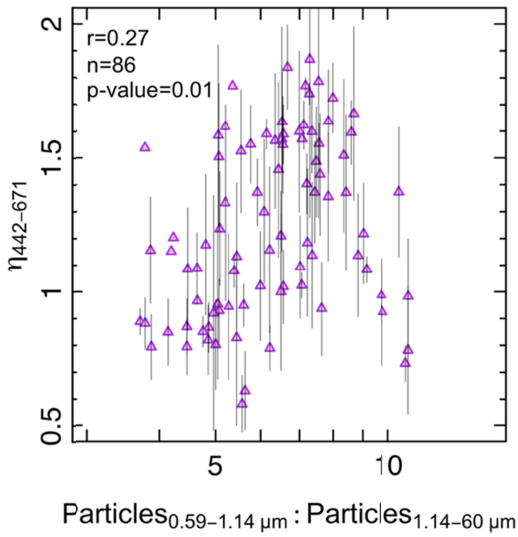


**Fig. S7.** The slope of the particulate optical backscattering coefficient ($b_{bp}$) computed between 442 and 671 nm, $\eta_{442\text{-}671}$, as a function of the ratio between the abundances of particles with diameters between 0.59 and 1.14 µm and between 1.14 and 60 µm. Error bars (black vertical lines within each point) represent the standard deviation. Statistics for linear fits on the log-transformed ratios are shown (see Table S4). Only samples collected in the mesopelagic region are used.

**Table S5. Correlation coefficient (r), number of points (n) and p-value for linear fits between the slope of the particulate beam attenuation coefficient ($c_p$) and various log-transformed particle concentrations and ratios. Prokaryotes are defined as the sum of cyanobacteria and heterotrophic bacteria. Only samples collected in the mesopelagic region are used. $^{**}$highly significant; $^{*}$significant; $^{ns}$not significant.**

| Concentrations | r | n | p-value | Cruise |
|---|---|---|---|---|
| Particles 0.6-60 µm | 0.35 | 15 | $0.20^{ns}$ | AMT26 |
| Particles 0.6-1.14 µm | 0.31 | 15 | $0.26^{ns}$ | AMT26 |
| Particles 1.14-60 µm | 0.40 | 15 | $0.13^{ns}$ | AMT26 |
| Particles 1.4-42 µm | 0.35 | 15 | $0.20^{ns}$ | AMT26 |
| Prokaryotes | 0.18 | 15 | $0.52^{ns}$ | AMT26 |
| Cyanobacteria | 0.17 | 15 | $0.56^{ns}$ | AMT26 |
| Eukaryotes | 0.21 | 13 | $0.50^{ns}$ | AMT26 |

| Ratios | r | n | p-value | Cruise |
|---|---|---|---|---|
| Particles 0.6-1.14 µm : Particles 1.14-60 µm | -0.03 | 15 | $0.91^{ns}$ | AMT26 |
| Prokaryotes : Eukaryotes | -0.13 | 13 | $0.68^{ns}$ | AMT26 |
| Cyanobacteria : Eukaryotes | 0 | 13 | $0.99^{ns}$ | AMT26 |
| Particles 1.4-2µm : Particles 2-42µm | 0.27 | 15 | $0.32^{ns}$ | AMT26 |
| Pico-eukaryotes : Nano-eukaryotes | -0.04 | 12 | $0.89^{ns}$ | AMT26 |

**Table S6. Correlation coefficient (r), number of points (n) and p-value for linear fits between the slope of the particulate optical backscattering coefficient between 488 and 550 nm, $\eta_{488\text{-}550}$, and log-transformed quantities of various particle concentrations and ratios. Prokaryotes are defined as the sum of cyanobacteria and heterotrophic bacteria. Only samples collected at 5 m and at the level of the deep chlorophyll maximum are used. $^{**}$highly significant; $^{*}$significant; $^{ns}$not significant.**

| Concentrations | r | n | p-value | Cruise |
|---|---|---|---|---|
| Particles 0.6-60 µm | -0.09 | 47 | $0.54^{ns}$ | AMT26 |
| Particles 0.6-1.14 µm | -0.08 | 47 | $0.59^{ns}$ | AMT26 |
| Particles 1.14-60 µm | -0.39 | 77 | $<0.01^{**}$ | AMT22, AMT26 |
| Prokaryotes | 0.06 | 73 | $0.60^{ns}$ | AMT22, AMT26 |
| Cyanobacteria | -0.05 | 76 | $0.69^{ns}$ | AMT22, AMT26 |
| Eukaryotes | -0.28 | 76 | $<0.01^{**}$ | AMT22, AMT26 |

| Ratios | r | n | p-value | Cruise |
|---|---|---|---|---|
| Particles 0.6-1.14 µm : Particles 1.14-60 µm | 0.08 | 47 | $0.59^{ns}$ | AMT26 |
| Prokaryotes : Eukaryotes | 0.38 | 71 | $<0.01^{**}$ | AMT22, AMT26 |
| Cyanobacteria : Eukaryotes | 0.18 | 76 | $0.12^{ns}$ | AMT22, AMT26 |

**Table S7. Correlation coefficient (r), number of points (n) and p-value for linear fits between the slope of the particulate optical backscattering coefficient between 488 and 550 nm, $\eta_{488\text{-}550}$, and log-transformed quantities of various particle concentrations and ratios. Prokaryotes are defined as the sum of cyanobacteria and heterotrophic bacteria. Only samples collected in the mesopelagic region are used. $^{**}$highly significant; $^{*}$significant; $^{ns}$not significant.**

| Concentrations | r | n | p-value | Cruise |
|---|---|---|---|---|
| Particles 0.6-60 µm | 0.14 | 86 | $0.19^{ns}$ | AMT26 |
| Particles 0.6-1.14 µm | 0.13 | 86 | $0.22^{ns}$ | AMT26 |
| Particles 1.14-60 µm | 0.14 | 86 | $0.19^{ns}$ | AMT26 |
| Prokaryotes | 0.18 | 20 | $0.46^{ns}$ | AMT26 |
| Cyanobacteria | -0.08 | 20 | $0.73^{ns}$ | AMT26 |
| Eukaryotes | 0.13 | 18 | $0.62^{ns}$ | AMT26 |

| Ratios | r | n | p-value | Cruise |
|---|---|---|---|---|
| Particles 0.6-1.14 µm : Particles 1.14-60 µm | 0.04 | 86 | $0.71^{ns}$ | AMT26 |
| Prokaryotes : Eukaryotes | -0.07 | 18 | $0.77^{ns}$ | AMT26 |
| Cyanobacteria : Eukaryotes | -0.28 | 18 | $0.27^{ns}$ | AMT26 |

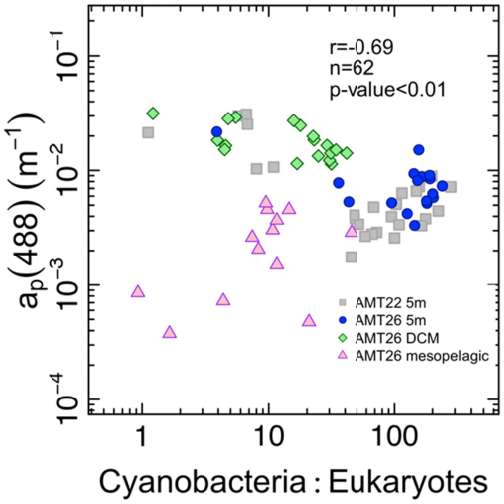


**Fig. S8.** Relationship between the particulate light absorption coefficients ($a_p$) at 488 nm and the ratio between the concentrations of cyanobacteria and eukaryotic phytoplankton. Statistics for linear fits on log-transformed quantities are shown and refer only to samples collected at 5 m and at the level of the DCM.

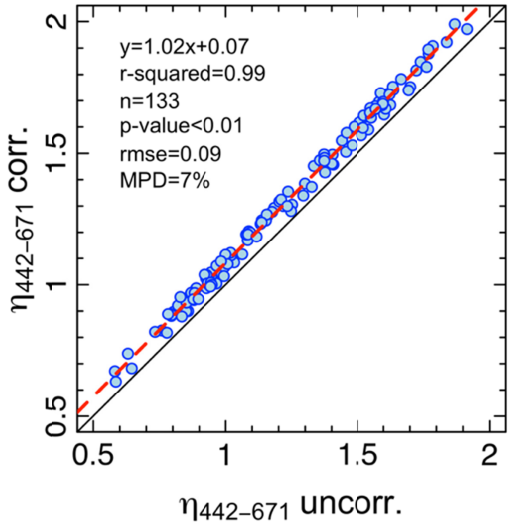


**Fig. S9.** Comparison between the slope of the particulate optical backscattering coefficient ($b_{bp}$) computed between 442 and 671 nm, $\eta_{442\text{-}671}$, before and after application of the so-called σ-correction (Table S1). The solid line represents the 1:1 ratio. The dashed line is the linear fit to all data. Statistics for the linear fit, root mean square error (RMSE) and median percentage difference (MPD) are shown. Only samples collected during the AMT26 cruise from surface to the mesopelagic region are used.